Growth and Photoluminescence of Crystalline $Si_{1-x}Ge_x/Si$ and $Si_{1-x-y}Ge_xC_y/Si$ Heterostructures

Anthony Andeol St. Amour

A DISSERTATION
PRESENTED TO THE FACULTY
OF PRINCETON UNIVERSITY
IN CANDIDACY FOR THE DEGREE
OF DOCTOR OF PHILOSOPHY

RECOMMENDED FOR ACCEPTANCE
BY THE DEPARTMENT OF
ELECTRICAL ENGINEERING

NOVEMBER 1996

© Copyright 1996 by Anthony Andeol St. Amour

All rights reserved

To my mother and father.

I have reached the top of this mountain,

only because they carried me from the bottom.

Abstract

We have measured and modeled, both analytically and numerically, the temperature dependence of the luminescence intensity in strained $Si_{1-x}Ge_x/Si$ (001) heterostructures. The high-temperature ($T > 150$ K) $Si_{1-x}Ge_x$ photoluminescence (PL) intensity in high-quality material is limited by recombination at the top Si surface, and this intensity can be dramatically increased by passivating the top surface with oxide. Also, due to Auger recombination suppressing the low temperature PL, we achieved essentially constant PL intensity from 77 to 250 K at high pump power density (30 W/cm^2). We have identified two causes for the observed difference in the temperature dependence of photo- and electroluminescence.

By Rapid Thermal Chemical Vapor Deposition, we have formed device quality pseudomorphic $Si_{1-x-y}Ge_xC_y$ thin films on Si (001), containing up to 1.2% substitutional carbon. The band gap of these strained films, as measured by PL, increased +21 meV/%C, and we predict that the band gap of *relaxed* $Si_{1-x-y}Ge_xC_y$ *decreases* -20 meV/%C. Also, we have demonstrated that, for a given band gap, $Si_{1-x-y}Ge_xC_y$ has less strain and a greater critical thickness than does $Si_{1-x}Ge_x$. We have fabricated $Si_{1-x-y}Ge_xC_y$ *p-i-n* diodes, which, for [C] $< 1.0\%$, showed no degradation in reverse-bias leakage compared to C-free devices. The infrared absorption spectra of these diodes showed increased sub-band gap absorption as the carbon content was increased

Acknowledgements

The former and current members of Prof. Sturm's research group who have contributed to my education and research are too numerous to acknowledge individually. I thank them all. Outside of our group, there are several individuals to whom I am indebted for their assistance. Yves Lacroix and Prof. Mike Thewalt of Simon Fraser University supported me with numerous photoluminescence measurements. Dan Quiram of Princeton's Chemical Engineering Department performed much of the X-ray diffraction used to characterize the strain in my $Si_{1-x-y}Ge_xC_y$ layers. Helena Gleskova and Vladimir Bulović of Princeton's Electrical Engineering Department provided valuable assistance with the *p-i-n* diode photoresponse measurements.

Working with Prof. Sturm has been a pleasure. His enthusiasm for research is infectious, and his obvious concern for the development of his students is gratefully appreciated. Indeed, all of the faculty members in the EMD group are extrordinary for their dedication to research and their keen interest in their students. Special thanks go to Profs. Kahn and Wagner for reading this thesis.

Contents

Abstract iv

1 Introduction 1

1.1 Motivation . . 1

Thesis Outline 2

2 Pseudomorphic $Si_{1-x}Ge_x$ on Si 4

2.1 Introduction 4

2.2 Effect of Biaxial Compression on the Band Structure of $Si_{1-x}Ge_x$ 5

Critical Thickness of Biaxially Compressed $Si_{1-x}Ge_x$ 7

2.4 Summary 12

3 Band-Edge Luminescence in Si and $Si_{1-x}Ge_x$ 13

3.1 Introduction 13

3.2 Radiative Recombination . . 14

3.3 Excitons and Electron-Hole Plasmas 17

3.4 Non-radiative Recombination 17

Luminescence Intensity 18

Summary 22

4 Temperature Dependence of $Si_{1-x}Ge_x$ Luminescence 23

4.1 Introduction 23

Qualitative View of Temperature Dependence . 23

Experimental Results and Analytical Model . . 25

4.4 Numerical Simulation 34

4.5 Pump Power Density Dependence 40

4.6 Temperature Dependence of Electroluminescence 45

4.7 Summary 53

5 Pseudomorphic $Si_{1-x-y}Ge_xC_y$ Alloys on Si (001) 54

5.1 Introduction 54

5.2 Carbon in Silicon 55

5.2.1 Solid solubility and diffusion 55

5.2.2 Measuring substitutional carbon 58

5.3 Previous Work 59

5.4 Rapid Thermal CVD of $Si_{1-x-y}Ge_xC_y$ 61

5.5 Summary 65

6 Optical and Electrical Properties of $Si_{1-x-y}Ge_xC_y$ 68

6.1 Photoluminescence Spectra 68

6.2 Band Gap of $Si_{1-x-y}Ge_xC_y$ 69

6.3 Towards Zero Strain 75

6.4 $Si_{1-x-y}Ge_xC_y$ *p-i-n* Diodes 83

6.4.1 Diode Fabrication 83

6.4.2 Diode I-V 83

6.4.3 Photoresponse 85

6.5 Summary 93

7 Conclusion 94

7.1 Summary 94

7.2 Future Work 95

References 96

A Medici Input Files 107

B Growth Sequences 111

B.1 $Si_{1-x-y}Ge_xC_y$ PL Sample #1740 112

B.2 $Si_{1-x-y}Ge_xC_y$ *p-i-n* Sample #1876 118

C Publications and Presentations Resulting from this Thesis 124

List of Figures

2.1 Lattice constants of relaxed and strained $Si_{1-x}Ge_x$ 6

2.2 Band gaps of relaxed and strained $Si_{1-x}Ge_x$ . . . 8

Trade-off between band gap and critical thickness 11

3.1 Photoluminescence spectrum of a $Si_{0.8}Ge_{0.2}$/Si quantum well 16

3.2 Radiative recombination probability for $Si_{0.8}Ge_{0.2}$ 21

4.1 Band diagram and p and n for photoluminescence simulation at 100 K 26

Band diagram and p and n for photoluminescence simulation at 250 K 27

4.3 Simulated pn product at 100 K and 250 K 28

4.4 Photoluminescence spectra of $Si_{0.3}Ge_{0.7}$ at various temperatures 30

4.5 Integrated photoluminescence intensity . 33

PL intensity and simulated pn without oxide 37

PL intensity and simulated pn with and without oxide 39

PL intensity for thick and thin Si caps 41

4.9 Comparison of PL intensity at high and low pump power 42

4.10 Simulated effective lifetime at high and low pump power 44

Simulated EL structure 47

4.12 Comparison of PL and EL intensity 48

4.13 Comparison PL and EL intensity at the same injection rate 49

4.14 Hole density in an EL simulation at 200 K 51

4.15 Simulated pn temperature dependence for various $W_{Si,eff}$. 52

5.1 Solid solubility and diffusion coefficients of C in Si 56

$Si_{1-x-y}Ge_xC_y$ X-ray diffraction spectra . 63

C fraction measured by XRD 64

5.4 SIMS profile of $Si_{1-x-y}Ge_xC_y$ 66

5.5 Growth rate of $Si_{1-x-y}Ge_xC_y$ films 67

6.1 PL spectra of $Si_{1-x-y}Ge_xC_y$ 70

6.2 Change in band gap of strained $Si_{1-x-y}Ge_xC_y$ 72

6.3 Band gap of relaxed $Si_{1-x-y}Ge_xC_y$ 76

6.4 Band gap as a function of strain 77

6.5 Critical thickness vs. composition 79

6.6 Critical thickness vs. band gap offset 80

6.7 PL from relaxed $Si_{1-x}Ge_x$ and strained $Si_{1-x-y}Ge_xC_y$ . . . 81

6.8 Defect etch of relaxed $Si_{1-x}Ge_x$ and strained $Si_{1-x-y}Ge_xC_y$ 82

6.9 *P-i-n* diode device structure . . 84

6.10 *P-i-n* diode I-V curves 86

6.11 *P-i-n* diode I-V curves for y=1.0% 87

6.12 Photoresponse of $Si_{1-x-y}Ge_xC_y$ *p-i-n* diodes 90

6.13 Photoresponse of all-Si diode 91

6.14 Photoresponse of $Si_{1-x-y}Ge_xC_y$ *p-i-n* diodes 92

Chapter 1

Introduction

1.1 Motivation

$Si_{1-x}Ge_x$ technology has matured rapidly over the past decade. Within the next few years, heterojunction bipolar transistors with strained $Si_{1-x}Ge_x$ bases may find use in high frequency analog and mixed-signal integrated circuits. Unfortunately, all other applications of $Si_{1-x}Ge_x$ are not so well developed. This is largely due to the properties of $Si_{1-x}Ge_x$ itself. For example, because the band gap of $Si_{1-x}Ge_x$ can be adjusted for the technologically important wavelengths of 1.3 and 1.55 μm, it has potential for use in infrared emitters and detectors. However, like its constituent elements, $Si_{1-x}Ge_x$ is an indirect band gap semiconductor and, therefore, is not an efficient band-to-band emitter or absorber. Furthermore, $Si_{1-x}Ge_x$ is not lattice matched to Si; pseudomorphic $Si_{1-x}Ge_x$ on Si is under biaxial compressive strain. Consequently, the thickness of pseudomorphic $Si_{1-x}Ge_x$ films is limited to their critical thickness. The strain for $x = 0.25$ is about 1%, and the equilibrium critical thickness is 10 nm[1, 2]. Clearly, this imposes a severe design constraint on strained $Si_{1-x}Ge_x$/Si heterostructures and will limit their application.

This thesis addresses both of these shortcomings of $Si_{1-x}Ge_x$. The first portion of this work treats the temperature dependence of the luminescence intensity from strained $Si_{1-x}Ge_x$/Si heterostructures. The second portion discusses the growth and

opto-electronic properties of a new material, $Si_{1-x-y}Ge_xC_y$, which shows potential for strain-free heterostructures on Si.

1.2 Thesis Outline

Chapter 2 serves as an introduction to strained $Si_{1-x}Ge_x$ on Si (001). The effect of biaxial compression on the band gap of $Si_{1-x}Ge_x$ is reviewed, and the concept of critical thickness is visited.

Chapter 3 discusses photoluminescence in Si and in $Si_{1-x}Ge_x$. The discussion briefly reviews band-edge photoluminescence line shapes, and an expression for the intensity of the luminescence is given.

Chapter 4 deals with the temperature dependence of photo- and electroluminescence intensity in strained $Si_{1-x}Ge_x$/Si heterostructures. We experimentally identify the origin of the temperature dependence of photoluminescence intensity and show that the intensity at room temperature can be increased dramatically by surface passivation. Furthermore, this behavior is shown to be well reproduced by a commercial numerical device simulator coupled to the luminescence model given in Chapter 3. In addition, electroluminescence simulations are performed and the results are used to explain the previously measured difference between photo- and electroluminescence temperature dependence.

Chapter 5 serves as an introduction to $Si_{1-x-y}Ge_xC_y$ ternary alloys on Si (001) substrates. First, we offer some background material on dilute C in Si, and a review of significant earlier work on $Si_{1-x-y}Ge_xC_y$ alloys is presented. Then, we discuss our method of chemical vapor deposition of $Si_{1-x-y}Ge_xC_y$, and its characterization by X-ray diffraction and SIMS.

Chapter 6 examines the opto-electronic properties of $Si_{1-x-y}Ge_xC_y$ ternary alloys. We use the photoluminescence spectra from pseudomorphic $Si_{1-x-y}Ge_xC_y$ on Si (001

to directly measure the effect of C on the band gap of strained $Si_{1-x-y}Ge_xC_y$ and to infer the band gap of relaxed $Si_{1-x-y}Ge_xC_y$. For a given band gap, the addition of C is shown to decrease the strain in the films and, consequently, increase the critical thickness. Chapter 6 then goes on to discuss the fabrication and characterization of $Si_{1-x-y}Ge_xC_y$ *p-i-n* diodes.

Lastly, Chapter 7 summarizes the contributions of this thesis and makes some suggestions for future work.

Chapter 2

Pseudomorphic $Si_{1-x}Ge_x$ on Si

2.1 Introduction

Si and Ge share the diamond crystal structure and are completely miscible, forming the random alloy $Si_{1-x}Ge_x$, whereby each lattice site is occupied by a Ge atom with probability x and by a Si atom with probability $1-x$. In the simplest approximation, the properties of $Si_{1-x}Ge_x$ are taken as the weighted average of the properties of Si and Ge. In this model then, the lattice constant (in Å) of $Si_{1-x}Ge_x$ is $a_{SiGe}(x) = a_{Si}(1-x) + a_{Ge}x = 5.432 + 0.225x$, whereas the actual lattice constant[3] is better fit by $a_{SiGe}(x) = 5.4315 + 0.1981x + 0.00282x^2$. The small quadratic term implies that the weighted average is a reasonable first-order approximation. We shall see later that this framework, called the virtual crystal model, is not so successful in describing the opto-electronic properties of $Si_{1-x-y}Ge_xC_y$ alloys.

The important point to note is that a_{SiGe} is larger than a_{Si}, about 1% larger for $x = 0.25$. If $Si_{1-x}Ge_x$ is deposited on Si, this lattice parameter mismatch may result in a high density of misfit dislocations at the $Si_{1-x}Ge_x$/Si interface. Dislocations are generally very efficient carrier recombination/generation sites, and therefore material with a high concentration of dislocations is not suitable for minority carrier devices such as bipolar transistors and *pn* junction diodes. However, if the $Si_{1-x}Ge_x$ is bi-axially compressed so that its in-plane lattice constant $a_{||}$ equals a_{Si}, there are no

dislocations at the interface. This configuration is termed commensurate or pseudomorphically strained. The vertical lattice constant $a_\perp$ expands according to elasticity theory, such that

$$a_\perp(x) = a_{SiGe}(x)\left[\quad \frac{2C_{12}(x)}{\quad} \frac{a_{Si} - a_{SiGe}(x)}{a_{SiGe}(x)}\right] \qquad (2.\ )$$

where $C_{11}(x)$ and $C_{12}(x)$ are the elastic constants of $Si_{1-x}Ge_x$ and are linearly interpolated between Si and Ge[4]. The relaxed $Si_{1-x}Ge_x$ lattice parameter a_{SiGe} and the strained $Si_{1-x}Ge_x$ lattice parameters are plotted in Fig. 2.1. Once the lattice constants are known (by X-ray diffraction, for example), such expressions as in Fig. 2.1 can be used to determine the alloy's composition

2.2 Effect of Biaxial Compression on the Band Structure of $Si_{1-x}Ge_x$

Relaxed $Si_{1-x}Ge_x$ has a cubic crystal structure, while the commensurately strained $Si_{1-x}Ge_x$ described in the previous section has a tetragonal structure ($a_\perp > a_{SiGe} > a_{||}$). Not surprisingly then, relaxed $Si_{1-x}Ge_x$ and strained $Si_{1-x}Ge_x$ have different electronic band structures. Conventionally, the effects of strain on the band structure of semiconductors are described by deformation potentials, which have units of energy/unit strain. Each band will have several deformation potentials, each describing a different type of strain (uniaxial, hydrostatic, shear, and so forth). Van de Walle[4, 5] linearly interpolated the deformation potentials of $Si_{1-x}Ge_x$ and computed the valence and conduction band structure of $Si_{1-x}Ge_x$ under various strain conditions.

For our present purposes, we are interested only in the condition where $Si_{1-x}Ge_x$ is commensurately strained to Si (001), and we will review those results now. First, the six-fold degenerate conduction band (CB) valleys along the Δ axes are split by

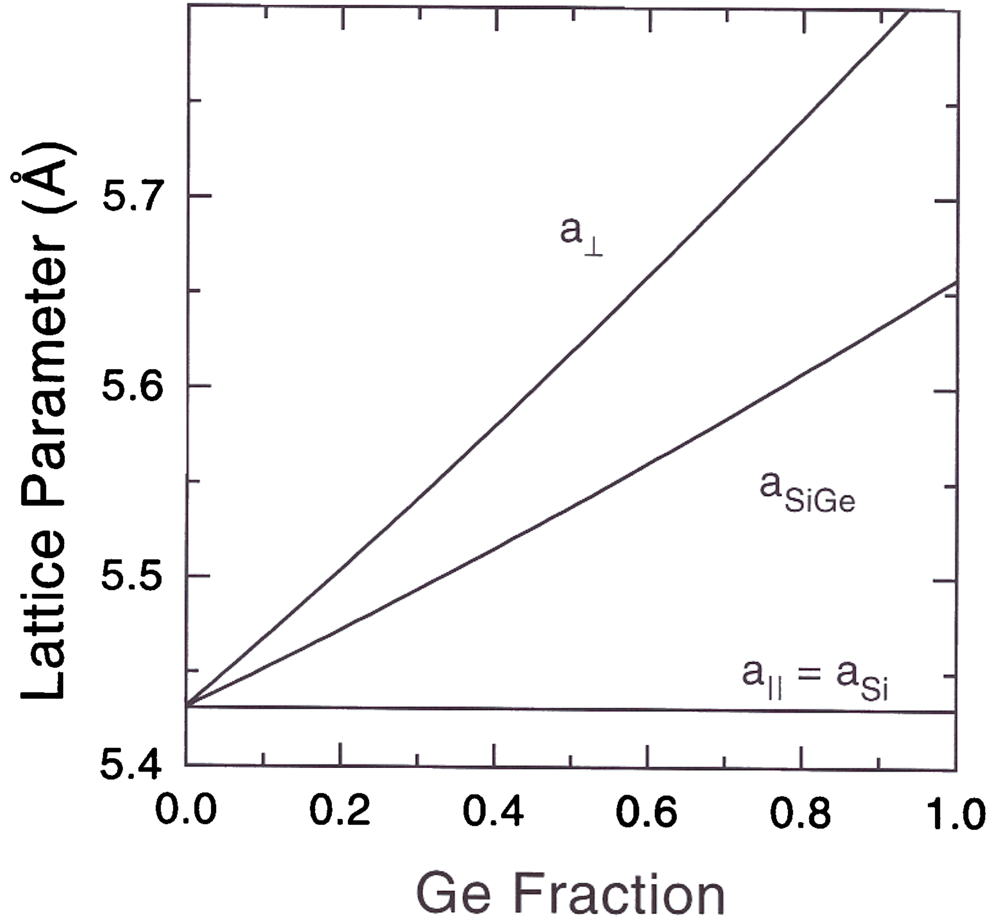

Figure 2.1: Lattice constant of relaxed $Si_{1-x}Ge_x$ and the lattice constants of pseudomorphic $Si_{1-x}Ge_x$ on Si (001) as a function of Ge fraction. The lattice constant of the relaxed material (a_{SiGe}) is a quadratic fit to the data of Dismukes *et al.*[3], and the strained lattice constant normal to the growth plane ($a_\perp$) was computed according to Eqn. 2.1. The in-plane lattice constant ($a_{||}$) equals the lattice constant of bulk Si (a_{Si}).

the biaxial compression, with two ([001] and [00$\bar{1}$]) going up relative to the other four ([100], [$\bar{1}$00], [010], and [0$\bar{1}$0]), which become the CB minima. The valence band (VB) maxima of Si, Ge, and relaxed $Si_{1-x}Ge_x$ all are four-fold degenerate at the Γ point. Under biaxial compressive strain, the bands split into two two-fold degenerate bands (heavy hole and light hole) with the heavy hole band as the new VB maximum. The fundamental indirect band gap of commensurately strained $Si_{1-x}Ge_x$ on Si (001) then is measured between the lowered four-fold CB minima and the raised two-fold heavy-hole VB maxima. The net result is that the band gap of $Si_{1-x}Ge_x$ is reduced by ~117 meV per percent biaxial compressive strain. For example, pseudomorphic $Si_{0.8}Ge_{0.2}$ has a strain of 0.84%, and its band gap is 98 meV below that of relaxed $Si_{0.8}Ge_{0.2}$. To further illustrate the effect of strain on the band gap of $Si_{1-x}Ge_x$, we have plotted in Fig. 2.2 the band gaps of both relaxed[6] and strained[7] $Si_{1-x}Ge_x$. Significantly deeper quantum wells in Si can be achieved with strained $Si_{1-x}Ge_x$ as compared to relaxed $Si_{1-x}Ge_x$.

The exact band alignment[8] at the strained $Si_{1-x}Ge_x$/Si heterojunction remains an open area of investigation. Specifically, it is not clear whether the $Si_{1-x}Ge_x$ CB minima are above or below those in Si. What is clear, however, is that the VB offset accounts for at least 90% of the band gap difference between Si and strained $Si_{1-x}Ge_x$.

2.3 Critical Thickness of Biaxially Compressed $Si_{1-x}Ge_x$

In the previous two sections, we saw that for heterojunction device applications strained $Si_{1-x}Ge_x$ has two distinct advantages over relaxed $Si_{1-x}Ge_x$: no misfit dislocations and a smaller band gap. The strain condition of a given $Si_{1-x}Ge_x$ film is determined by thermodynamic and kinetic considerations and depends on the film's composition, thickness, and the thermal budget to which it has been exposed.

Because Si and Ge are similar (same valence and crystal structure), a coherent

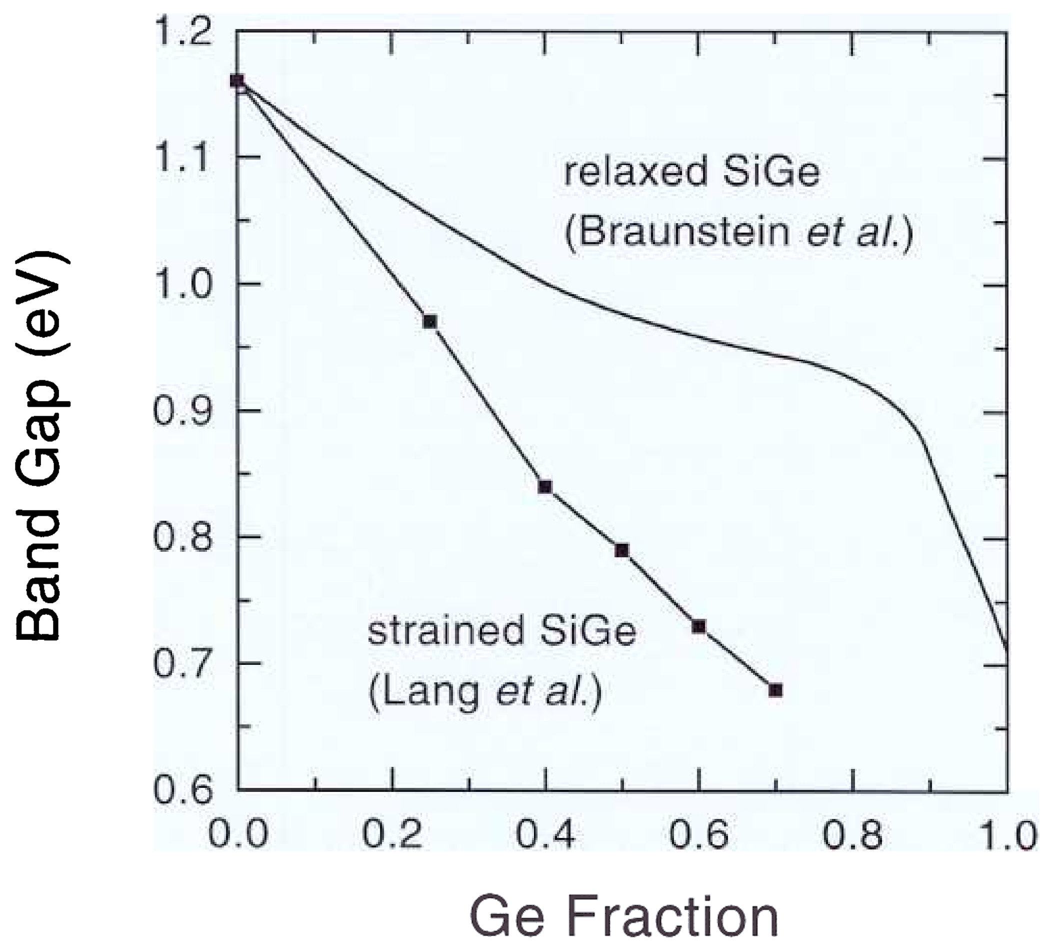

Figure 2.2: Band gap of relaxed and strained $Si_{1-x}Ge_x$ as a function of Ge fraction. The relaxed band gap is a fit to the data of Braunstein *et al.*[6], and the strained band gap is the data of Lang *et al.*[7]. Both were measured by optical absorption.

interface between Si and $Si_{1-x}Ge_x$ has a negligibly small energy associated with it[9, 10]. On the other hand, an interface between relaxed $Si_{1-x}Ge_x$ and Si is decorated with many misfit dislocations, which do have a significant energy associated with them. The initial growth mode for $Si_{1-x}Ge_x$ on Si is commensurate, thus avoiding the energy cost of dislocations. However, there is an elastic energy proportional to the thickness of the film associated with the strain in the $Si_{1-x}Ge_x$. Above a certain thickness (called the critical thickness) this strain energy exceeds the dislocation energy and the relaxed film becomes thermodynamically stable. Below the critical thickness, the strained film is unconditionally stable. Furthermore, the strain in the film (and thus the strain energy) increases with Ge fraction so that critical thickness decreases as Ge fraction increases.

Matthews and Blakeslee[1, 11] derived an expression for the critical thickness of strained epitaxial thin films, which has been applied to $Si_{1-x}Ge_x$[2, 12]. Although strained $Si_{1-x}Ge_x$ is not isotropic, the derivation is done with isotropic elasticity theory because there is no simple anisotropic theory to treat dislocations. Bear in mind that the total lattice parameter misfit f between the thin film ($Si_{1-x}Ge_x$) and the substrate (Si) in general is accommodated by a combination of plastic strain δ and elastic strain ϵ.

$$f \quad \frac{\Delta a}{a_{Si}} \quad \delta + \epsilon$$

According to isotropic elasticity theory, the dislocation energy is

$$E_{dis} \quad \frac{2\delta}{\quad} \frac{Gb^2(1-\nu\cos^2\theta)}{4\pi(1-\nu)} \ln\frac{\alpha h}{b} \quad \delta K_1 \ln\frac{\alpha h}{b}$$

where G is the shear modulus; ν is Poisson's ratio; b is the Burger vector; θ is the angle between the dislocation line and its Burger vector; λ is the angle between the Burgers vector and the direction in the interface normal to the dislocation line; α is the core parameter; and h is the layer thickness.

The strain energy in the isotropic limit is

$$E_{strain} \quad 2G\frac{1+\nu}{1-\nu}\epsilon^2 h \equiv K_2\epsilon^2 h$$

Minimizing the total energy $E_{total} = E_{dis} + E_{strain}$ with respect to elastic strain, yields the thermal equilibrium elastic strain

$$\epsilon_{equil} = \frac{K_1}{2K_2}\frac{\ln\frac{\alpha h}{b}}{h}$$

From Eqn. 2.5 we see that for thick films ($h \gg \ln h$), the equilibrium elastic strain is near zero and all of the misfit is taken up by plastic deformation (i.e., dislocations). On the other hand, when the elastic strain equals the total misfit, there are no dislocations. Consequently, the equilibrium critical thickness for the onset of dislocation formation is defined as the point where $\epsilon_{equil} = f = 0.042x$. For $Si_{1-x}Ge_x$, the Matthews-Blakeslee equilibrium critical thickness h_c[1, 2] (in Å) is defined by

$$x = 5.5\frac{\ln\frac{\alpha h_c}{b}}{h_c}$$

In Fig. 2.3, we have plotted, as a function of Ge fraction, both the Matthews-Blakeslee critical thickness and the band gap difference compared to Si for fully strained $Si_{1-x}Ge_x$ This figure demonstrates the trade-off between h_c and ΔE_G. Applications at 1.3 μm, for example, require $E_G = 950$ meV which corresponds to a strained $Si_{1-x}Ge_x$ film with $x = 0.2$ at room temperature. The equilibrium critical thickness for that film is only 130 Å, clearly a serious constraint. A mitigating factor, however, is that dislocation-free $Si_{1-x}Ge_x$ films whose thicknesses exceed the equilibrium critical thickness are routinely grown. By low-temperature, Rapid Thermal Chemical Vapor Deposition, we have grown 20% Ge films which showed no evidence of relaxation to thicknesses exceeding 500 Å. Attempts have been made to define a "metastable critical thickness,"[13, 14] but experiments have shown that it depends on the exact thermal budget to which the film has been exposed and the experiment's sensitivity to dislocations.

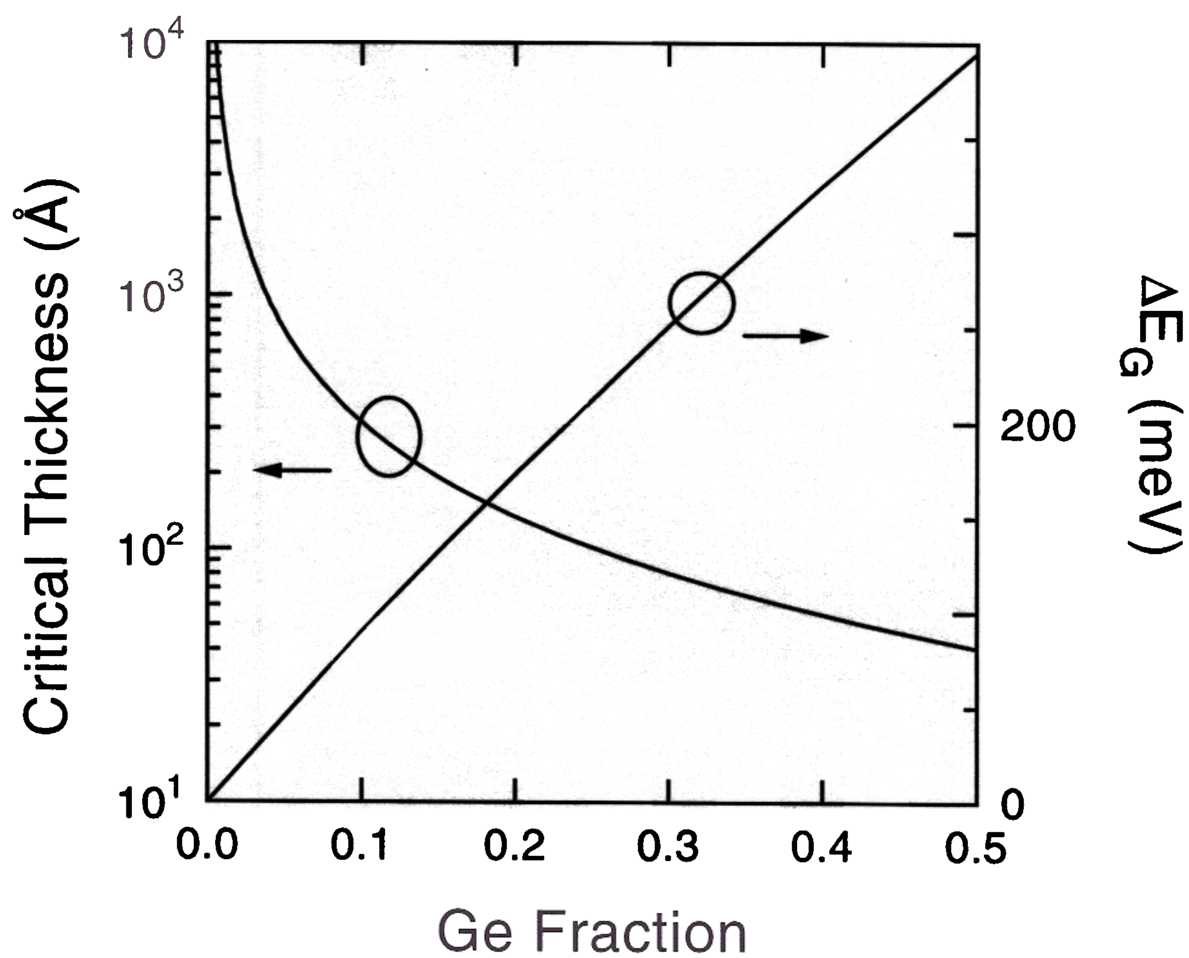

Figure 2.3: Matthews-Blakeslee equilibrium critical thickness and ΔE_G as a function of Ge fraction.

2.4 Summary

Biaxial compressive strain in $Si_{1-x}Ge_x$ layers grown commensurately on Si (001) has two important consequences which we shall revisit in Chapters 5 and 6 when $Si_{1-x-y}Ge_xC_y$ alloys are treated:

1. The strain reduces the band gap of $Si_{1-x}Ge_x$.

2. The strain introduces a finite critical thickness.

Chapter 3

Band-Edge Luminescence in Si and $Si_{1-x}Ge_x$

3.1 Introduction

A comprehensive investigation of photoluminescence in relaxed bulk $Si_{1-x}Ge_x$ alloys was reported by Weber and Alonso[15] in 1989. Several excitonic recombination processes were identified, including no-phonon and phonon-assisted recombination. The intensity ratios of the different lines were shown to be determined by the alloy's composition, and the energies of the momentum-conserving phonons and the band gap energy were measured. In 1991, Sturm *et al.*[16] reported the first well-resolved band-edge PL from fully strained $Si_{1-x}Ge_x$ quantum wells grown on Si. This work showed that the luminescence from strained $Si_{1-x}Ge_x$ is essentially similar to that from relaxed material, with the only significant difference being a shift to lower energy due to the band gap reduction caused by the strain. In the past five years, photoluminescence has become one of the most popular characterization techniques for Ge/Si heterostructures. It is used to measure the band gap; and, because its intensity is determined largely by non-radiative defect-related recombination, PL is widely used as a tool for determining the quality of epitaxial heterostructures and for optimizing epitaxial growth. Furthermore, as bright PL is viewed as the first step towards efficient Si-based light emitting diodes (LEDs), PL studies have been used to evaluate novel heterostructures thought to be useful in LEDs.

In this chapter, we will briefly discuss the $Si_{1-x}Ge_x$ band-edge PL spectrum and the important radiative and non-radiative recombination processes which determine the PL intensity. Also, we will derive a temperature dependent expression for the radiative recombination probability in $Si_{1-x}Ge_x$, which will be used in the following chapter to model the temperature dependence of luminescence in $Si_{1-x}Ge_x$ heterostructures.

3.2 Radiative Recombination

Excess electrons and holes in Si and in $Si_{1-x}Ge_x$ recombine via several competing processes, each of which may be characterized by a lifetime τ. These processes may be divided into two groups: radiative and non-radiative recombination. The processes of direct interest to us are the radiative ones, those in which a photon is emitted to conserve energy. In the case of band-to-band recombination, a conduction band (CB) electron recombines with a valence band (VB) hole and the emitted photon has energy approximately equal to that of the material's band gap. However, these materials have indirect band gaps; their CB minima and VB maxima lie at different points in momentum space. Because photons carry little momentum, another process must accompany photon emission to conserve momentum. The strongest such process in Si is the emission of a transverse optical (TO) phonon, which has an energy of 58 meV. Thus, the brightest luminescence line in Si lies 58 meV below its band gap energy. The emitted photon energy will be further reduced by the exciton binding energy ($\sim$15 meV) if the luminescence is due to excitons rather than to free electrons and holes and by the exciton-impurity binding energy ($\sim$4 meV) if the excitons are bound to impurities.

In addition to phonon emission, another momentum conserving process is available in indirect band gap random alloys. Recall that $Si_{1-x}Ge_x$ is a random alloy in

that each lattice site is randomly occupied by a Ge atom with probability x and by a Si atom with probability $1 - x$. This randomness removes the translational symmetry which is the origin of the requirement of crystal momentum conservation in perfect crystal lattices, allowing the indirect transition to proceed without phonon participation. The efficiency of this process, called alloy scattering[17, 18], is proportional to $x(1 - x)$ and is comparable to that of TO phonon emission. The resulting no-phonon (NP) luminescence line[15] lies at the band gap of the $Si_{1-x}Ge_x$ and, as will be shown later, can be used as a measure of the band gap. Figure 3.1 shows a photoluminescence (PL) spectrum of a single pseudomorphic $Si_{0.8}Ge_{0.2}$ film with a Si cap on a Si (001) substrate. The spectrum was measured at 77 K under excitation by 514 nm light from an Ar ion laser. The three luminescence peaks, from low to high energy, are the $Si_{1-x}Ge_x$ TO replica, the $Si_{1-x}Ge_x$ no-phonon (NP) peak, and the Si TO replica. The Si NP line is absent because no scattering mechanism comparable to alloy scattering in the $Si_{1-x}Ge_x$ is available.

Si and $Si_{1-x}Ge_x$ may also exhibit luminescence which is not due to the band-edge phenomena discussed above. The recombination may be mediated by a luminescent defect. Dislocations in Si, for example, have been identified as the origin of several PL lines (called D-lines) lying below the band gap[19]. Also, sub-band gap PL has been observed in certain $Si_{1-x}Ge_x$ samples grown by molecular beam epitaxy[20], and the responsible defect is thought to be related to radiation damage[21] but has yet to be positively identified. Generally, luminescent features other than the band-edge NP line and phonon replicas are undesired as they indicate the presence of defects in the material.

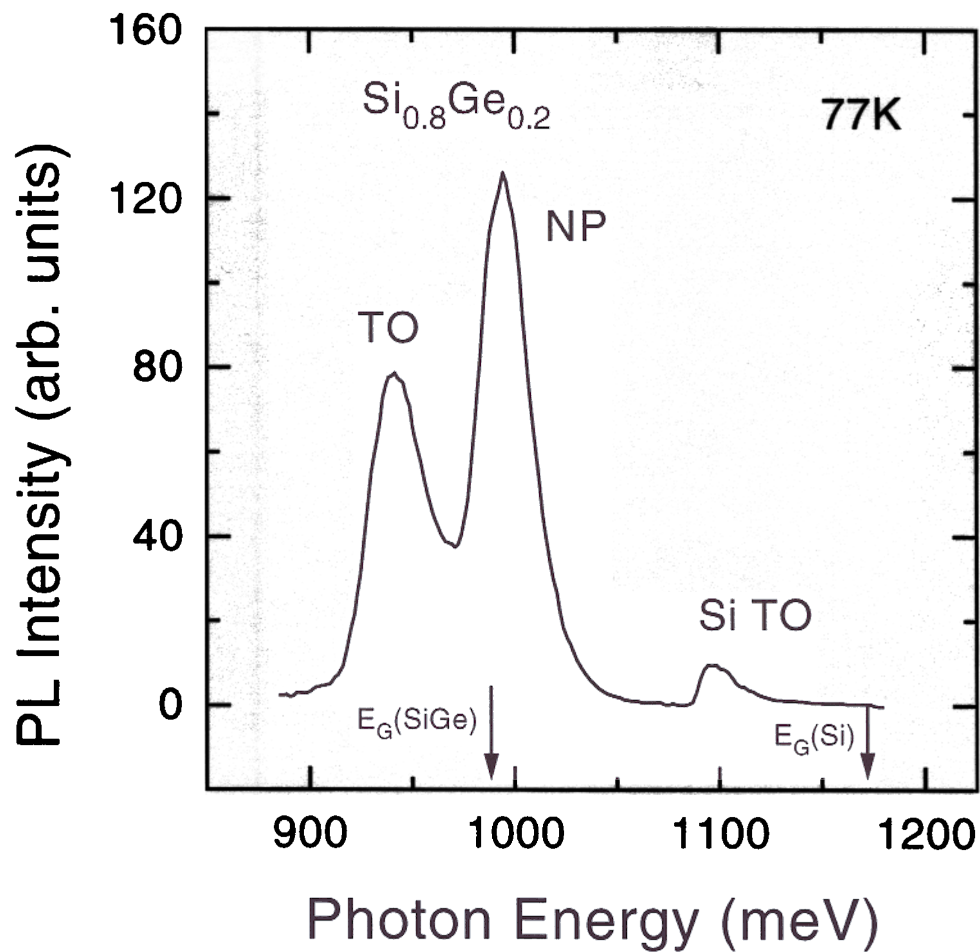

Figure 3.1: PL spectrum of a $Si_{0.8}Ge_{0.2}$/Si quantum well measured at 77 K.

3.3 Excitons and Electron-Hole Plasmas

Band-edge luminescence in Si and $Si_{1-x}Ge_x$ as discussed in the previous section may be due to bound excitons (BE), free excitons (FE), or an electron-hole plasma (EHP). These three modes (BE, FE, and EHP) may be distinguished by looking at the luminesence lineshapes. At very low temperatures ($T < 10$ K), the excitons in Si and $Si_{1-x}Ge_x$ are bound to impurities and the luminescence exhibits a symmetric lineshape[22]. At higher temperatures, the excitons are free to move and the luminescence is due to either free excitons[16] or an electron-hole plasma[23]. The classic FE lineshape[22, 15] is the product of the exciton density of states and the Boltzmann function

$$I_{FE}(h\nu) \propto \sqrt{h\nu - E_0} \cdot e^{-(h\nu - E_0)/kT} \quad (3.1)$$

$$E_0 \quad E_G \quad \hbar\omega \quad E_{FE} \quad (3.2)$$

where $h\nu$ is the photon energy, $\hbar\omega$ is the phonon energy (if relevant), and E_{FE} is the exciton binding energy (15 meV for Si and 4 meV for Ge[22]). At high carrier densities and elevated temperature, the PL is due to an EHP rather than to discrete excitons. The EHP signature is a broader line than Eqn. 3.1 of the FE. EHP[24, 23, 25] luminescence spectra are given by a convolution of the free electron and hole densities of states and the electron and hole Fermi functions. Based on such lineshape analysis and on the associated carrier concentration, the $Si_{1-x}Ge_x$ PL in Fig. 3.1, and indeed all high temperature PL measured for this thesis, was assumed to be due to electron-hole plasmas. We shall return to this point in Chap. 4 when we discuss the temperature dependence of the luminescence intensity.

Non-radiative Recombination

As their name implies, non-radiative processes do not emit a photon to conserve energy. For example, in the case of Auger recombination, the energy liberated by one

electron relaxing from the conduction band (CB) to the valence band (VB) is given to either another CB electron or a VB hole. Our experience also suggests that defects related to excess oxygen result in non-radiative recombination whereby the energy is delivered to the lattice. At moderate carrier concentrations (i.e., below the regime where Auger recombination becomes important), the non-radiative lifetime $\tau_{non-rad}$ is determined by defects and impurities in Si and $Si_{1-x}Ge_x$. Because the band-edge radiative process is second order, requiring phonon emission or alloy scattering, the radiative lifetime τ_{rad} is many orders of magnitude larger than $\tau_{non-rad}$. Thus, the total effective lifetime in the sample is determined by non-radiative recombination and is defined as

$$\tau_{eff} = \frac{1}{P_{total}} \int \acute{n} \cdot dV \tag{3.3}$$

where P_{total} is the total photogeneration rate, $\acute{n}$ is the excess free carrier density, and the integral is computed over the entire sample. The effective lifetime, then, is a weighted average of all recombination processes, including Shockley-Hall-Read, Auger, and surface recombination

Luminescence Intensity

Ignoring reabsorption, the luminescence intensity per unit area[26] in Si and $Si_{1-x}Ge_x$ is given by

$$I \quad \int Bnp \cdot dx \tag{3.4}$$

where n and p are the electron and hole concentrations, B is the radiative recombination probability, and the integral is evaluated over the region of interest. Important points to note are: (1) B is a material property and is most generally a function of n, p, and T, and (2) n and p are determined jointly by the generation rate (pump power) and the predominantly non-radiative defect-mediated recombination mechanisms mentioned in the previous section. Schlangenotto *et al.*[26] derived an

expression for B in Si The key elements of that derivation are repeated here.

Coulomb attraction between an electron and a hole increases their probability of being at the same position and, thus, being candidates for recombination. For a given two-particle state s in the hole's reference frame, this probability is the product of the expectation value of the electron concentration at the position of the hole, $n_s(0)$, and the expectation value of the hole concentration p_s. It is important to note that, due to Coulomb attraction, $n_s(0)p_s$ is larger than the product of the mean concentrations, $n_s p_s$. The recombination rate for state s is

$$R_s = B_0 n_s(0) p_s \tag{3.5}$$

The internal recombination probability B_0 is assumed to be the same for all states including excitons and was obtained by Dumke[27] for the indirect radiative band-to-band recombination of free electrons and holes:

$$B_0 \quad \frac{4\pi\epsilon\hbar^3 E_G^2 A}{c^2(m_{de}m_{dh})^{3/2}} \coth\frac{\hbar\omega}{2kT} \quad C\coth\frac{\hbar\omega}{2kT}$$

where $\hbar\omega$ is the phonon energy, m_i are the density of states effective masses, A is a constant occurring in corresponding expressions for absorption, and the coth factor is due to the participation of a single type of phonon. Rigorously, there should be a separate term for each phonon type (TO, TA, etc.).

To explicitly evaluate $n_s(0)p_s$, the wavefunction of the state s is required. Schlangenotto used the radial solution $\Phi_s(r)$ of the hydrogen-like Schrödinger equation of the electron-hole system. Summing over all states including excitons yields the total recombination rate R

$$R \quad B_0 \sum n_s(0) p_s \quad B_0 \left(\sum_{band} \Phi_s(0) \,|^2\, n_s p_s + \sum_{exciton} \Phi_s(0) \,|^2\, n_{ex,s} \right)$$

where $n_{ex,s}$ is the density of excitons in state s Using Boltzmann statistics, Schlangenotto explicitly evaluated Eqn. 3.7 for the case of spherical bands in which the

conduction band minimum was displaced from the valence band maximum in k-space (i.e., an indirect semiconductor). In this case, both $n_s p_s$ and $n_{ex,s}$ are proportional to np so that $R = B \cdot np$, and to a good approximation B is given by

$$B_{Si} = 4\sqrt{\pi}\sqrt{\frac{G}{kT}}\left(1 + 2\frac{G}{kT}e^{G/kT}\right)\coth\left(\frac{\hbar\omega}{2kT}\right)C$$

where G is the exciton Rydberg energy. The "1" in the parentheses corresponds to band-to-band (or electron-hole plasma) recombination and is enhanced by the factor $4\sqrt{\pi}\sqrt{\frac{G}{kT}}$ compared to B_0 due to Coulomb attraction. The second term corresponds to exciton recombination, assuming only ground state excitons.

To apply Eqn. 3.8 to $Si_{1-x}Ge_x$, we must add a term for the no-phonon (NP) luminescence so that the $Si_{1-x}Ge_x$ radiative recombination coefficient is given by

$$B_{SiGe} = 4\sqrt{\pi}\sqrt{\frac{G}{kT}}\left(1 + 2\frac{G}{kT}e^{G/kT}\right)\left[\coth\left(\frac{\hbar\omega}{2kT}\right) + \eta_{NP}\right]C$$

At low temperature ($kT \ll \hbar\omega$), the coth term is very nearly one and $\eta_{NP} = I_{NP}/I_{TO}$, the NP-to-TO luminescence intensity ratio. The NP intensity is determined by alloy scattering, which is dependent on composition but not on temperature[28]. Venkataraman *et al.*[18] found that $I_{NP}/I_{TO} = 7.0x(1-x)$ at 77 K.

Equation 3.9 can be simplified for our purposes. First, note that the Si TO phonon energy $\hbar\omega$ is 58 meV so that the coth term is very nearly one for $T \leq 300$ K. Also, the PL spectra discussed in this thesis are due to electron-hole plasmas and, therefore, the exciton term does not apply. The relevant band-to-band radiative recombination probability then is

$$B_{SiGe,bb} = 4\sqrt{\pi}\sqrt{\frac{G}{kT}}\left[1 + \eta_{NP}\right]C \tag{3.10}$$

B_0 (Eqn. 3.6), B_{SiGe} (Eqn. 3.9) and $B_{SiGe,bb}$ (Eqn. 3.10) are plotted as a function of temperature in Fig. 3.2. Much of the temperature dependence is eliminated with the exciton recombination term, but, as we will see in Chap. 4, the luminescence intensity remains strongly temperature dependent through $n(T)$ and $p(T)$.

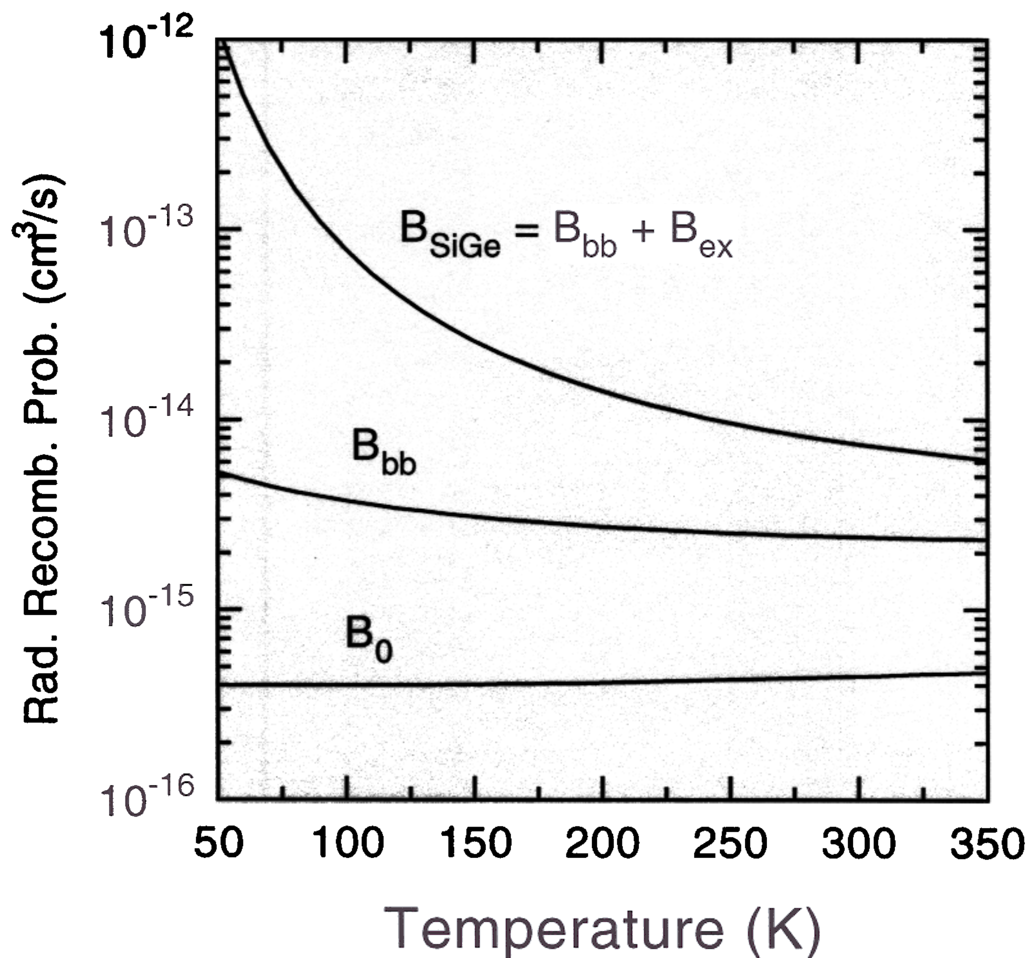

Figure 3.2: Radiative recombination probabilities for $Si_{0.8}Ge_{0.2}$ as a function of temperature based on the derivation of Schlangenotto *et al.*[26]. B_0 is the internal recombination probabilty, B_{bb} is the band-to-band recombination probabilty, and B_{SiGe} is the total recombination probability including band-to-band and excitonic recombination. The exciton Rydberg $G = 15$ meV, and $C = 4 \times 10^{-16}$ cm^3 s^{-1}.

3.6 Summary

Band-edge luminescence from $Si_{1-x}Ge_x$ is due to the recombination of conduction band electrons and valence band holes or excitons. The energy of the emitted photons depends on the band gap, and thus the composition, of the $Si_{1-x}Ge_x$, and therefore can be used to measure band gap and composition. The intensity of the luminescence is given by the product of pn and B, the radiative recombination probability. We shall see in the next chapter that the pn product, and thus the luminescence intensity, in the $Si_{1-x}Ge_x$ is determined by the temperature, pump power, and the recombination mechanisms operating within the sample. We shall also see that for our experiments B is largely independent of temperature.

Chapter 4

Temperature Dependence of $Si_{1-x}Ge_x$ Luminescence

Introduction

Most of the early reports regarding the luminescent properties of strained $Si_{1-x}Ge_x$/Si heterostructures discussed experiments performed at low temperatures, $T < 10$ K[29, 16, 30, 31]. More recently, though, there has been increased interest in luminescence at higher temperatures[32, 33, 34, 35]. This has been motivated both by the desire for room temperature emitters and because luminescence at high temperature has appeared to be a more severe test of material properties. But the physical origin of the temperature dependence of the luminescence intensity was not explained.

In this chapter we describe experiments in which the temperature dependence of the band-edge luminescence intensity in strained $Si_{1-x}Ge_x$/Si heterostructures was measured and modeled. The emphasis is on identifying the dominant mechanisms responsible for the temperature dependence of the $Si_{1-x}Ge_x$ luminescence intensity.

Qualitative View of Temperature Dependence

Band-edge luminescence in $Si_{1-x}Ge_x$ is due to the recombination of excess electrons and holes, and the intensity of that luminescence is given by Eqn. 3.4. In photolumi-

nescence (PL) experiments the excess electrons and holes are photogenerated by an optical pump, which has a characteristic absorption length. Our experiments were performed with an Ar ion laser tuned to 514 nm (2.41 eV), where the absorption length in Si is about 1 μm. As the thicknesses of our $Si_{1-x}Ge_x$ films were typically on the order of 100 Å, most of the absorption occurred in the Si substrate. The photogenerated carriers then diffused and were trapped in the low band gap $Si_{1-x}Ge_x$ quantum well.

Ignoring differences in densities of states and assuming Boltzmann statistics, the quasi-equilibrium carrier concentrations in the $Si_{1-x}Ge_x$ well and those in the Si cladding (substrate and cap) are related by

$$\frac{np(SiGe)}{np(Si)} \quad e^{\Delta E_G/kT}$$

where np is the product of the electron and hole densities in the respective materials and $\Delta E_G = E_{G,Si} - E_{G,SiGe}(x)$. Equation 4.1 is valid for non-degenerate carrier densities and flat quasi-Fermi levels. For $x = 0.2$, $\Delta E_G = 170$ meV so that at 77 K, $\frac{np(SiGe)}{np(Si)} = 1 \times 10^{11}$, an enormous number. However, at low temperature (T < 150 K), thermal diffusion of the carriers is not rapid enough to support quasi-equilibrium, and the actual electron and hole densities in the $Si_{1-x}Ge_x$ are lower than those predicted by Eqn. 4.1. Therefore, the carrier distributions and consequently the luminescence intensity is partially determined by kinetics, rather than solely by equilibrium. At 300 K, $\frac{np(SiGe)}{np(Si)}$ is a more reasonable 700 and diffusion is faster so that Eqn. 4.1 can be maintained. In this case, the carrier distributions and PL intensity are determined by quasi-equilibrium alone.

Figures 4.1 and 4.2 show the results of a numerically simulated PL experiment, the details of which are given in Section 4.4. We have plotted the electron and hole densities as well as the band diagrams for a single optically pumped $Si_{0.65}Ge_{0.35}$ quantum well (50 Å) at two temperatures: 100 K (Fig. 4.1) and 250 K (Fig. 4.2).

Recall that for strained $Si_{1-x}Ge_x$ on Si most of the band gap difference appears as a VB offset and the CB offset is very small (0 ± 10 meV). For these simulations, we took the CB offset to be zero so that all of the band gap difference appears in the VB. (Slightly adjusting the electron affinity in $Si_{1-x}Ge_x$ and thus adding a small ΔE_C had little effect on our results.) Because of the large VB offset (230 meV), there is considerable hole confinement in the $Si_{1-x}Ge_x$, resulting in orders of magnitude higher hole density in the $Si_{1-x}Ge_x$ compared to in the Si. This high hole density bends the bands and attracts electrons, especially at the lower temperature. At 100 K, the hole quasi-fermi level E_{fp} is not flat, indicating that the hole populations in the Si and in the $Si_{1-x}Ge_x$ are not in equilibrium. At 250 K, E_{fn} and E_{fp} are flat, indicating that both the electron and hole populations are in equilibrium.

In Fig. 4.3 we have plotted the pn product as a function of depth at 100 K and at 250 K. In both cases, $pn(SiGe)$ is much greater than $pn(Si)$; however, at 100 K the difference is considerably larger with essentially all of the photogenerated carriers in the $Si_{1-x}Ge_x$. Recall from Chap. 3 that the PL intensity (per unit area) is given by $I_{SiGe} = B(T) \int np \cdot dx$, and the radiative recombination probability B is a weak function of temperature in our range of interest. Based on this model of PL and on the simulated pn (Fig. 4.3), we expect the PL intensity at 100 K to be orders of magnitude more intense than that at 250 K. That is exactly what we will see in the next section.

4.3 Experimental Results and Analytical Model

Yves Lacroix of Simon Fraser University measured the photoluminescence spectra of two of our $Si_{1-x}Ge_x$ quantum well structures (#1539 and #1623) from 6 to 300 K. Sample #1539 contained a single 150 Å 20% Ge layer with a 200 Å Si cap. Sample #1623 contained a single 50 Å 30% Ge layer, also with a 200 Å cap. The pump

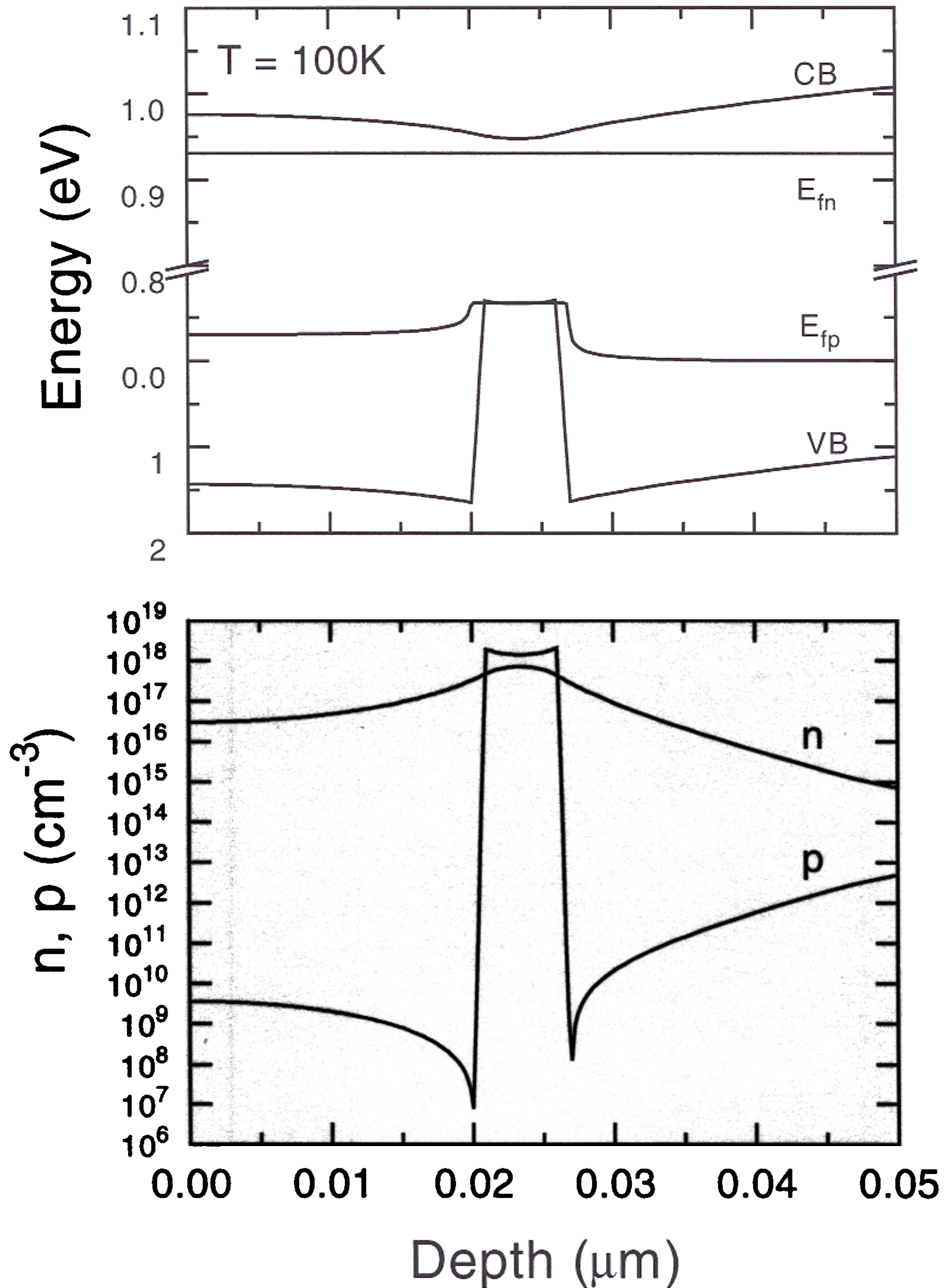

Figure 4.1: Band diagram and carrier concentrations as a function of depth for a photoluminescence simulation at 100 K. The photogeneration rate was 4.2×10^{17} $cm^{-2}s^{-1}$, and the pump absorption length was 1 μm. The top Si surface recombination velocities (S_n and S_p) were 3×10^4 cm/s.

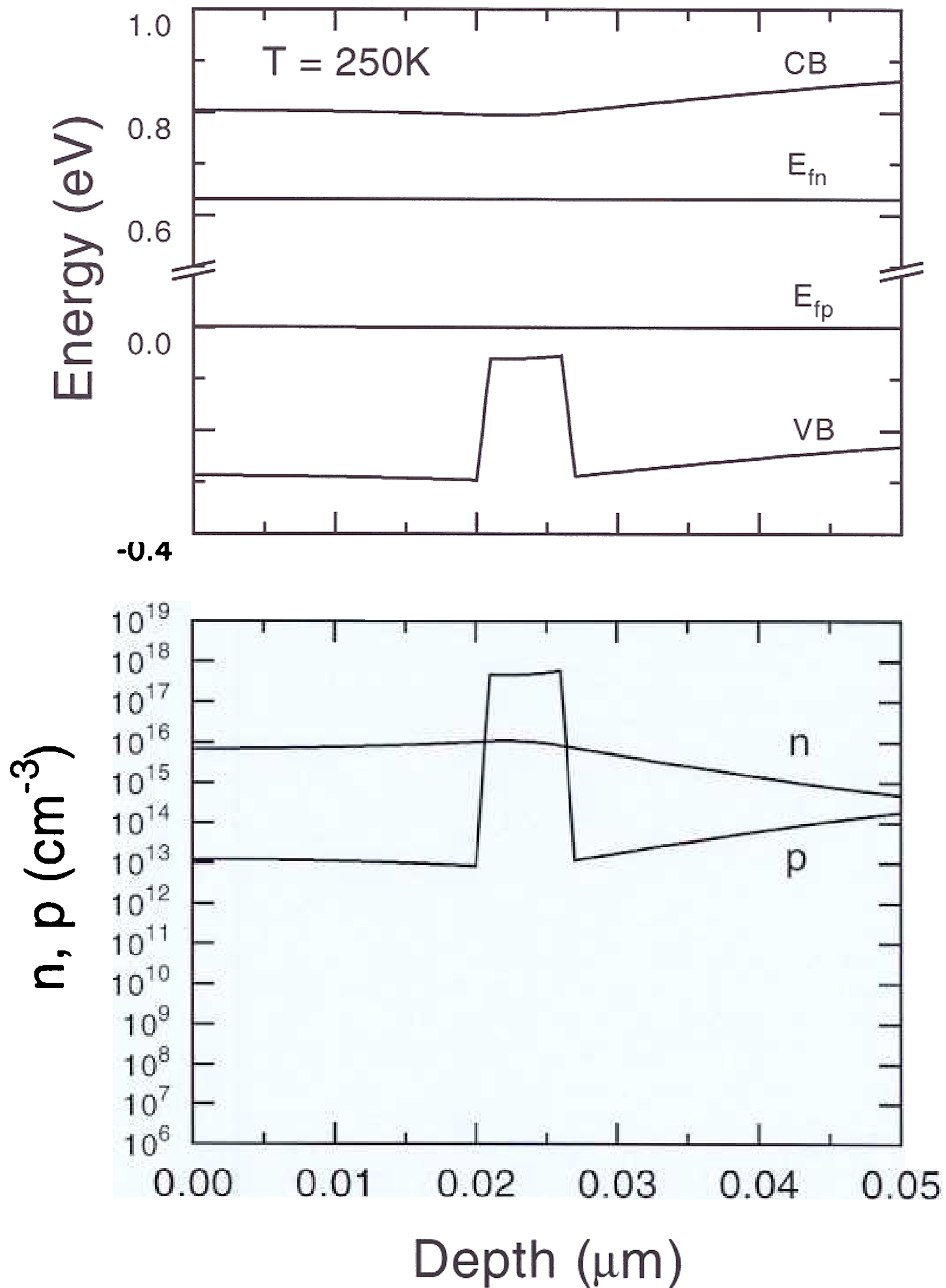

Figure 4.2: Band diagram and carrier concentrations as a function of depth for a photoluminescence simulation at 250 K. The photogeneration rate was 4.2×10^{17} $cm^{-2}s^{-1}$, and the pump absorption length was 1 μm. The top Si surface recombination velocities (S_n and S_p) were 3×10^4 cm/s.

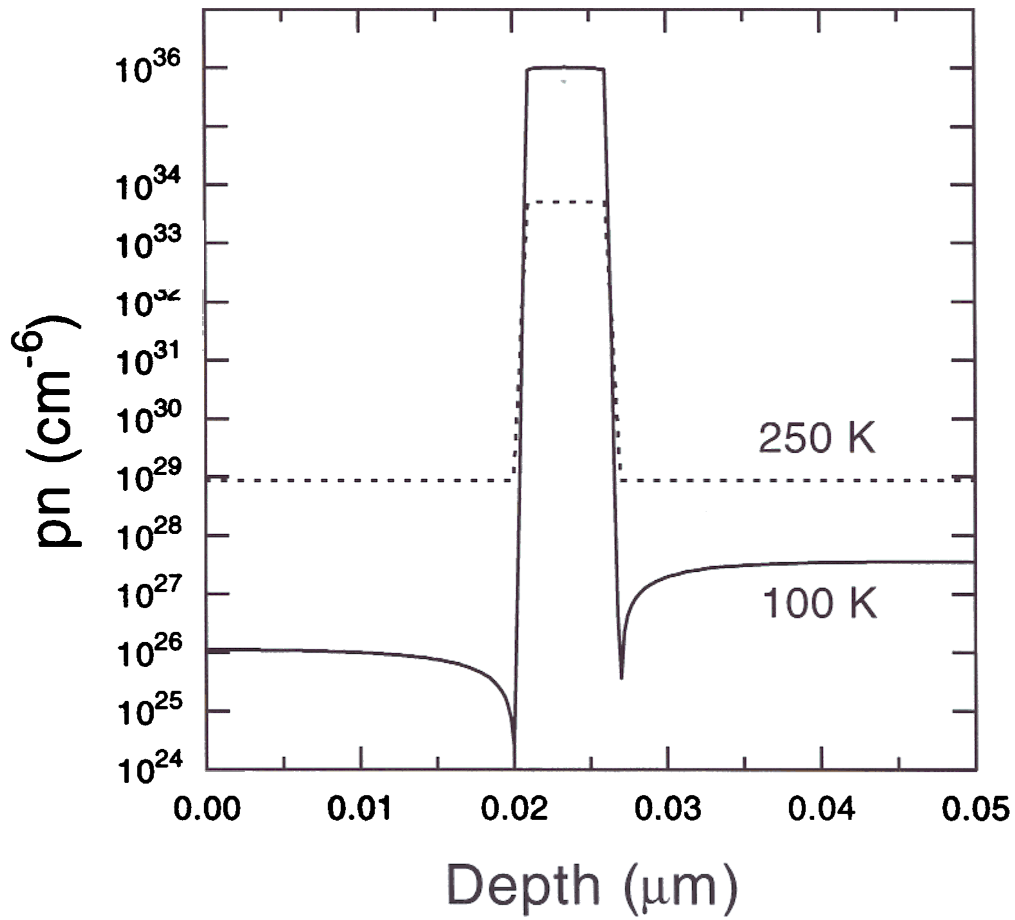

Figure 4.3: Simulated *pn* product as a function of depth for 100 K and 250 K. The photogeneration rate was 4.2×10^{17} $cm^{-2}s^{-1}$, and the pump absorption length was 1 μm. The top Si surface recombination velocities (S_n and S_p) were 3×10^4 cm/s.

power density was ~0.3 W/cm^2. Fig. 4.4 shows several PL spectra measured from sample #1623 (30% Ge, 50 Å). As predicted earlier in this chapter, the intensity of the $Si_{1-x}Ge_x$ luminescence dropped sharply at higher temperatures ($T > 150$ K). A qualitatively similar temperature dependence of PL from as-grown $Si_{1-x}Ge_x$ quantum wells with Si caps has been observed by several other groups[32, 33, 35]. In the 6 K spectrum, the $Si_{1-x}Ge_x$ no-phonon (NP) line and the TO and TA replicas were observed, while no sub-band gap luminescence was observed[20, 21]. This is evidence of high-quality, uniform material. All lines above 1 eV originated in the Si substrate. Note that in the 6 K spectrum, the Si TO line had comparable intensity to the $Si_{1-x}Ge_x$ NP line but was cut off so as not to obscure the other spectra. The strength of the Si signal at very low temperature (compared to that above 80 K) is due to the inability of the photogenerated carriers to diffuse to the quantum well and to the fact that at this low temperature many carriers exist as excitons bound to impurities. We saw in Chap. 3 that excitons have a very high radiative recombination probability[26].

Above ~80 K, both the Si and the $Si_{1-x}Ge_x$ band-edge PL are due to electron-hole plasmas (EHP)[23, 24]. To see this in the Si, note that the Si TO feature in the 80 K spectra was shifted to slightly higher energy compared to at 6 K because it was no longer reduced by the exciton binding energy. (The shift back to lower energy as the temperature was increased was due to the reduction of the band gap with increased temperature.) Given that the carrier densities in the $Si_{1-x}Ge_x$ were in all cases much higher than those in the Si, one also expects that the $Si_{1-x}Ge_x$ PL was due to an EHP, rather than to free excitons (FE). Confirming this is the fact that the thermal broadening of our spectra could be well fit by the EHP lineshape model mentioned in Chap. 3 and, generally, that the carrier densities in the $Si_{1-x}Ge_x$ exceeded the Mott[36, 37] criteria for the transition from FEs to an EHP. Therefore, we ascribe our PL as that due to an EHP, rather than FEs.

The integrated PL intensity from both samples (#1539 and #1623) is plotted as

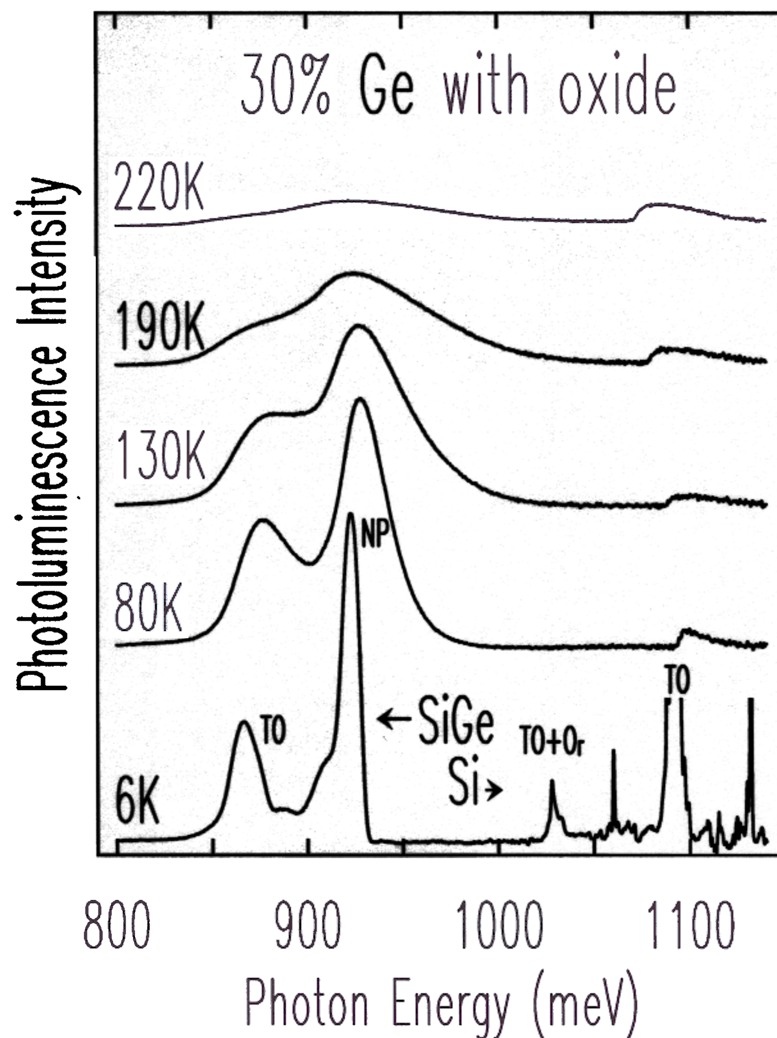

Figure 4.4: Five photoluminescence spectra from sample #1623 (30% Ge). The pump power density was ~ 0.3 W/cm^2. In the 6 K spectrum, the $Si_{1-x}Ge_x$ TA phonon replica appeared as a shoulder on the low-energy side of the NP line. The significance of "with oxide" is explained in Sec. 4.4.

a function of inverse temperature in Fig. 4.5. Notice that the PL intensity at low temperature was constant. In this regime, nearly all of the photogenerated carriers are trapped in the $Si_{1-x}Ge_x$ so that the $Si_{1-x}Ge_x$ luminescence is much stronger than that of the Si, and its absolute intensity is controlled by the excess carrier lifetime in the $Si_{1-x}Ge_x$ (a weak function of temperature) At elevated temperatures the PL intensity rolled off with an activation energy equal to the band gap difference between Si and $Si_{1-x}Ge_x$, as predicted by Eqn. 4.1. We shall see shortly that the temperature of the "knee" is determined by the various recombination mechanisms operating within the sample.

We have presented a phenomenological model[34] for the temperature dependence of photoluminescence. This model is based on thermal equilibrium (Eqn. 4.1) between the carriers in the Si and those in the $Si_{1-x}Ge_x$ and yields a result for the measured integrated intensity of the $Si_{1-x}Ge_x$ luminescence, I_{SiGe}

$$I_{SiGe} \quad \frac{C_1}{1+\gamma e^{-\Delta E_G/kT}}$$

$$\gamma = \frac{\tau_{SiGe} W_{Si}}{\tau_{Si} W_{SiGe}} \qquad ([illegible])$$

τ_{SiGe} is the lifetime in the $Si_{1-x}Ge_x$, and τ_{Si} is the effective lifetime in the Si (including recombination at the top surface). ΔE_G is the band gap difference between Si and the $Si_{1-x}Ge_x$. W_{SiGe} is the width of the $Si_{1-x}Ge_x$ layer, and W_{Si} is the effective width of the Si in which the photogenerated carriers reside. W_{Si} has an upper limit of the wafer thickness (500 μm) and a lower limit of the pump's absorption length (1 μm), and is generally on the order of the minority carrier diffusion length. This analytical model assumes that the effective lifetimes are not a function of temperature.

The model was fit to the data of Fig. 4.5. For sample #1623 (50 Å, 30% Ge), we obtained values of $\Delta E_G = 210$ meV and $\gamma = 1.5\times10^6$. For sample #1539 (150 Å, 20% Ge), we obtained ΔE_G 140 meV and γ 2.0×10^5. In both cases, the extracted ΔE_G was quite close to the value measured directly from the low temperature PL spectra.

The γ values are also quite close, and about half of their difference is due to the unequal $Si_{1-x}Ge_x$ layer thicknesses. The rest can easily be attributed to uncontrolled wafer-to-wafer variations in the concentration of trace nonradiative impurities in our samples such as oxygen unintentionally introduced during growth.

We will see later that a good estimate for W_{Si} is 100 μm. Plugging that into the above expression for γ (Eqn. 4.3), yields a lifetime ratio $\frac{\tau_{SiGe}}{\tau_{Si}} = 75$. Why is the excess carrier lifetime in the $Si_{1-x}Ge_x$ so much higher than that in the Si? Most of the Si consists of a lightly doped substrate and a high temperature (1000° C) epitaxial buffer, while the $Si_{1-x}Ge_x$ was grown at 625°C. Typical low-temperature epitaxial layers have a higher defect density than do layers grown at high temperature (> 800°C), partly because of less efficient desorption of oxygen-bearing species[38]. Based on this one would expect a *lower* lifetime in the $Si_{1-x}Ge_x$.

The model is very simple and contains only one truly free parameter (ΔE_G can be independently measured by the energy position of the NP line, for example) because all of the recombination and transport behavior is lumped into that one parameter, γ. Accurate modeling of the real problem must take into account the heterostructure, potentially unequal lifetimes in different materials (and at interfaces), band bending due to charge accumulation in the quantum well, complications due to high carrier densities (such as Auger recombination and degeneracy), the diffusion of the photogenerated carriers, and so forth. Given all that, we must feel fortunate that the simple analytical model worked so well, and we should not be surprised that it can not clarify this issue of the low lifetime in Si. For that we turned to a more complex numerical model, capable of simulating every effect.

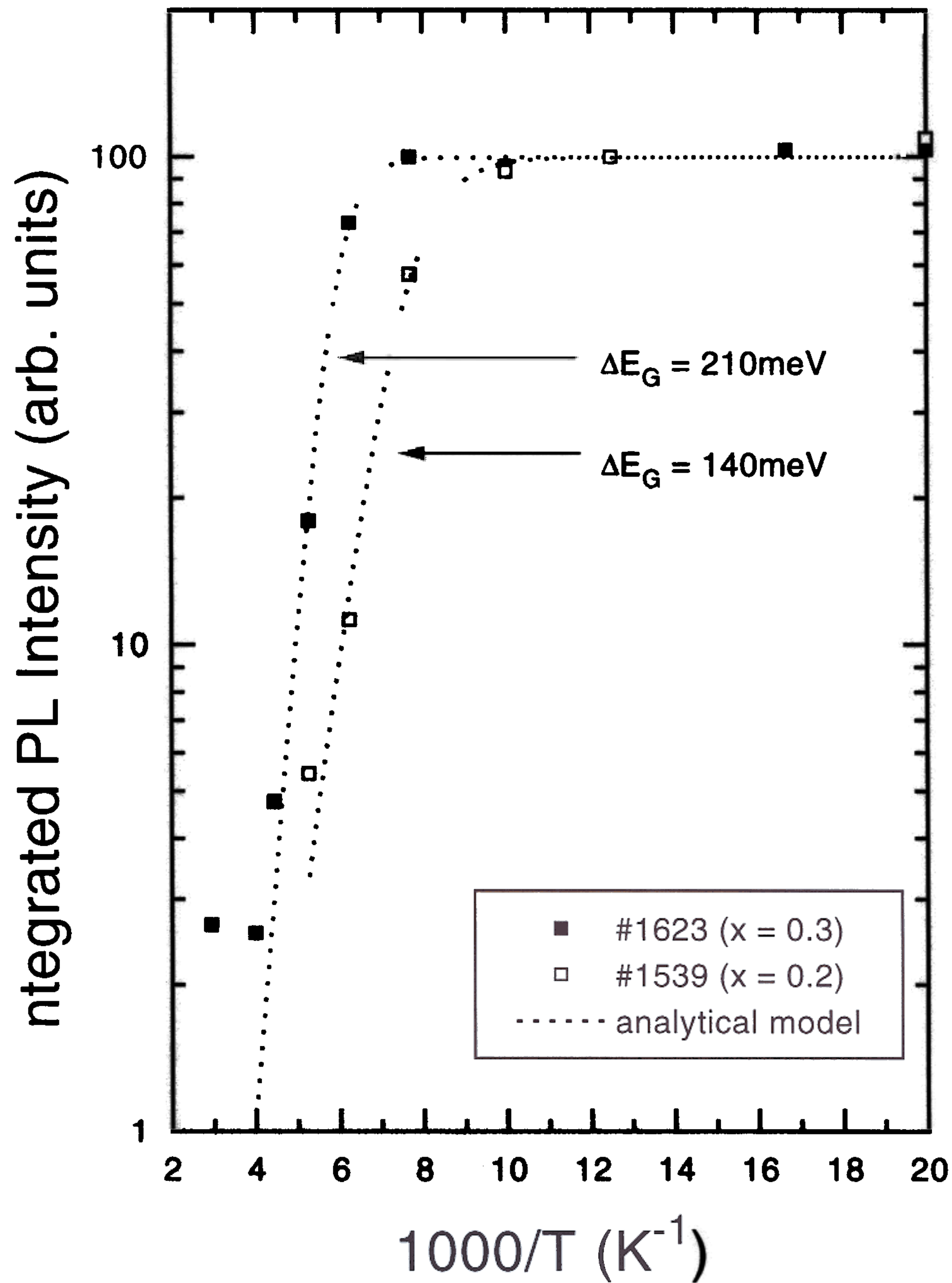

Figure 4.5: Integrated $Si_{1-x}Ge_x$ photoluminescence intensity as a function of inverse temperature.

4.4 Numerical Simulation

Our methodology for analyzing the temperature dependence of the $Si_{1-x}Ge_x$ luminescence was to compute the carrier concentrations as a function of temperature and pump power density (photogeneration rate), and then use Schlangenotto's luminescence model (Chap. 3) as a post-processor to generate luminescence intensity from the electron and hole profiles. We found, however, that the measured PL intensity was proportional to the simulated pn product, indicating that the radiative recombination probability B was constant for our experiments. In Chap. 3, we argued that for our case the temperature dependence of B was weak, coming only from the Coulomb attraction. The exciton term was not relevant, and the phonon factor was nearly 1 over our temperature range of interest. Now we will see that our data was well fit by eliminating the Coulomb attraction as well and taking B as a constant with respect to temperature. The absence of evidence of Coulomb attraction in our data may be due to screening[39] at our high carrier densities, especially at low temperature where the densities are highest in the $Si_{1-x}Ge_x$. From this point on, we will take B as a constant and directly compare the measured PL intensity to the simulated pn product.

The carrier concentrations were computed using the commercial two-carrier numerical semiconductor device simulator TMA MEDICI^{TM}. This program numerically solves Poisson's equation and the electron and hole continuity equations self-consistently for the electrostatic potential and the electron and hole concentrations. MEDICI has the ability to handle heterojunctions, optical absorption (via depth dependent photogeneration), and numerous models for carrier transport[40]. Our simulations included both Shockley-Hall-Read (SHR) and Auger recombination in the bulk and surface recombination at the top Si surface. Having assumed that radiative recombination was insignificant compared to non-radiative recombination, the bulk

TAUNO	TAUPO	AUGN	AUGP
1 μs	1 μs	2.8×10^{-31} cm^6/s	9.9×10^{-32} cm^6/s

Table 4.1: MEDICI recombination parameters.

recombination rate was given by

$$R = R_{SHR} + R_{Auger} \tag{4.4}$$

$$R_{SHR} = \frac{pn - n_i^2}{\texttt{TAUPO} \cdot (n + n_i) + \texttt{TAUNO} \cdot (p + n_i)} \tag{4.5}$$

$$R_{Auger} = \texttt{AUGN} \cdot (pn^2 - nn_i^2) + \texttt{AUGP} \cdot (np^2 - pn_i^2) \tag{4.6}$$

For simplicity, we chose the density of states, mobilities, SHR lifetimes (TAUPO and TAUNO), and Auger recombination coefficients (AUGN and AUGP) to be the same in Si and in $Si_{1-x}Ge_x$. The MEDICI recombination parameters used are given in Table 4.1. The effect of the top surface was included by selecting finite electron and hole recombination velocities. Appendix A shows two sample MEDICI input files: one for PL simulations and one for EL simulations.

On Fig. 4.6 we have simultaneously plotted the measured PL intensity from sample #1623 (30% Ge) and the simulated integrated *pn* product in $Si_{1-x}Ge_x$. The simulated *pn* accurately reproduced the behavior of the data: flat at low temperature and rolling off at higher temperature. However, our initial simulation, which did not include surface recombination, over-estimated the PL intensity for $T > 150$ K (solid line). Fitting the data required an additional recombination mechanism which became more significant at higher temperatures There are increasingly more carriers in the Si at high temperature so that decreasing the effective lifetime in the Si would better fit the data by reducing the high temperature PL without affecting the low temperature PL. The SHR lifetimes in Si and $Si_{1-x}Ge_x$ were already equal (1 μs), and there is no reason that the bulk lifetime should be *lower* in Si. However, top surface recombination does reduce the effective Si lifetime, and we found that by including equal electron and

hole surface recombination velocities $S_n = S_p = 3 \times 10^4$ cm/s we could fit our PL data.

The choice of 1 μs SHR lifetimes was not completely arbitrary. Rather, it was selected because, at the relevant pump power, it generated carrier densities roughly consistent with those obtained by fitting the measured PL spectra to the electron-hole plasma lineshape model. To test the effect of lifetime on our conclusions, simulations were run using various lifetimes. For $0.01 \leq \tau_{SHR} \leq 1$ μs, the total number of photogenerated carriers scaled exactly with $1/\tau_{SHR}$ in the absence of surface recombination at 300 K. And when τ_{SHR} was reduced by an order of magnitude from 1 to 0.1 μs, pn was diminished by 18× at 100 K and 5× at 250 K so that the "knee" temperature was raised slightly. In all, our conclusions do not depend strongly on the choice of τ_{SHR}.

The numerical simulation results are consistent with our analytical model. From the analytical model, we concluded that the effective lifetime in the Si was somehow lower than that in the $Si_{1-x}Ge_x$. The numerical simulation has shown that our experimental observations are consistent with top Si surface recombination being a significant recombination path at temperatures above ~150 K, leading to a lower effective lifetime in the Si.

That top surface recombination was indeed important was proved by thermally oxidizing our samples[41, 42]. Thermal oxidation is known to reduce the recombination velocity of Si surfaces. The 100 Å oxide was grown at 800°C for 10 minutes in steam following an RCA clean. The PL intensity from this oxide-passivated sample is compared to the unpassivated sample in Fig. 4.7. (Actually, the unpassivated sample was oxidized as well but had its oxide stripped by dilute HF. This way both samples received the same thermal treatment and an annealing effect of the oxidation was ruled out as a cause for our observations. The oxide passivation increased the high temperature PL intensity by over an order of magnitude compared to the unpassi-

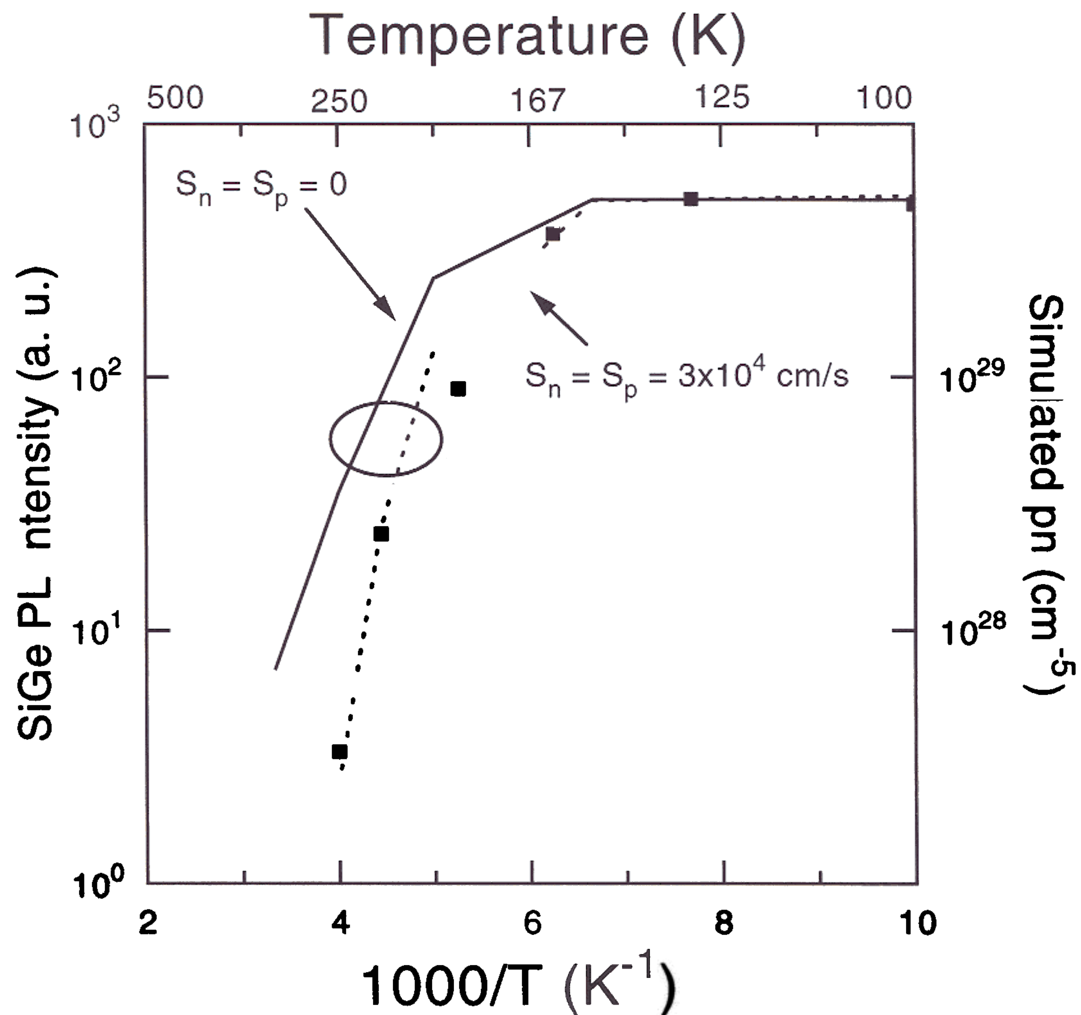

Figure 4.6: Measured integrated photoluminescence intensity and simulated *pn* as a function of inverse temperature. The squares are measured PL intensity, and the lines are simulated *pn*. The kinks in the simulated *pn* are the result of connecting discrete points with straight line segments. Each kink does not represent a critical temperature.

vated sample. The luminescence from the passivated sample was fit by simulations with $S_n = S_p \leq 10^3$ cm/s, indicating that oxidation decreased the recombination velocity by at least a factor of 30. For reference, high-quality MOS oxides typically have recombination velocities ~100 cm/s.

The analytical model was fit to the PL intensity of the oxide passivated samples, holding ΔE_G fixed at 210 meV and 140 meV for samples #1623 (30% Ge) and #1539 (20% Ge), respectively. With the oxide passivation, γ decreased from 1.5×10^6 to 1.8×10^5 for sample #1623; and from 2.0×10^5 to 1.0×10^4 for sample #1539. Of the factors in γ, only τ_{Si} could be affected by the presence of a surface oxide. We, therefore, conclude that oxide passivation increased the effective Si lifetime by a factor of 10-20. This is roughly consistent with the surface recombination velocity decreasing from 3×10^4 to 10^3 cm/s, as was found by numerical simulation.

Given that top surface recombination was just shown to be significant, one might expect the Si cap thickness to play a role in the rate of top surface recombination because it is the cap which separates the carriers in the $Si_{1-x}Ge_x$ quantum well from the top surface. However, it is important to recall that only at elevated temperatures (when there are significant carriers in the Si) does the top surface contribute to the overall recombination rate. In this high-temperature regime, the carrier distribution in the viscinity of the well is determined by equilibrium so that the cap thickness is important only if it impedes the flow of carriers to the Si surface. This can only be the case for cap thickness comparable to the diffusion length, which is on the order of 50 μm at 250 K. Therefore, for all reasonable PL structures, cap thinkness plays no role in the temperature dependence of the luminescence intensity. This was experimentally demonstrated by measuring the temperature dependence of the PL from a $Si_{0.8}Ge_{0.2}$ quantum well capped by 3800 Å of Si. Figure 4.8 shows that its temperature dependence was identical to that of the previous $Si_{0.8}Ge_{0.2}$ quantum well with the thin cap (200 Å). Also, as before, oxide passivation enhanced the high

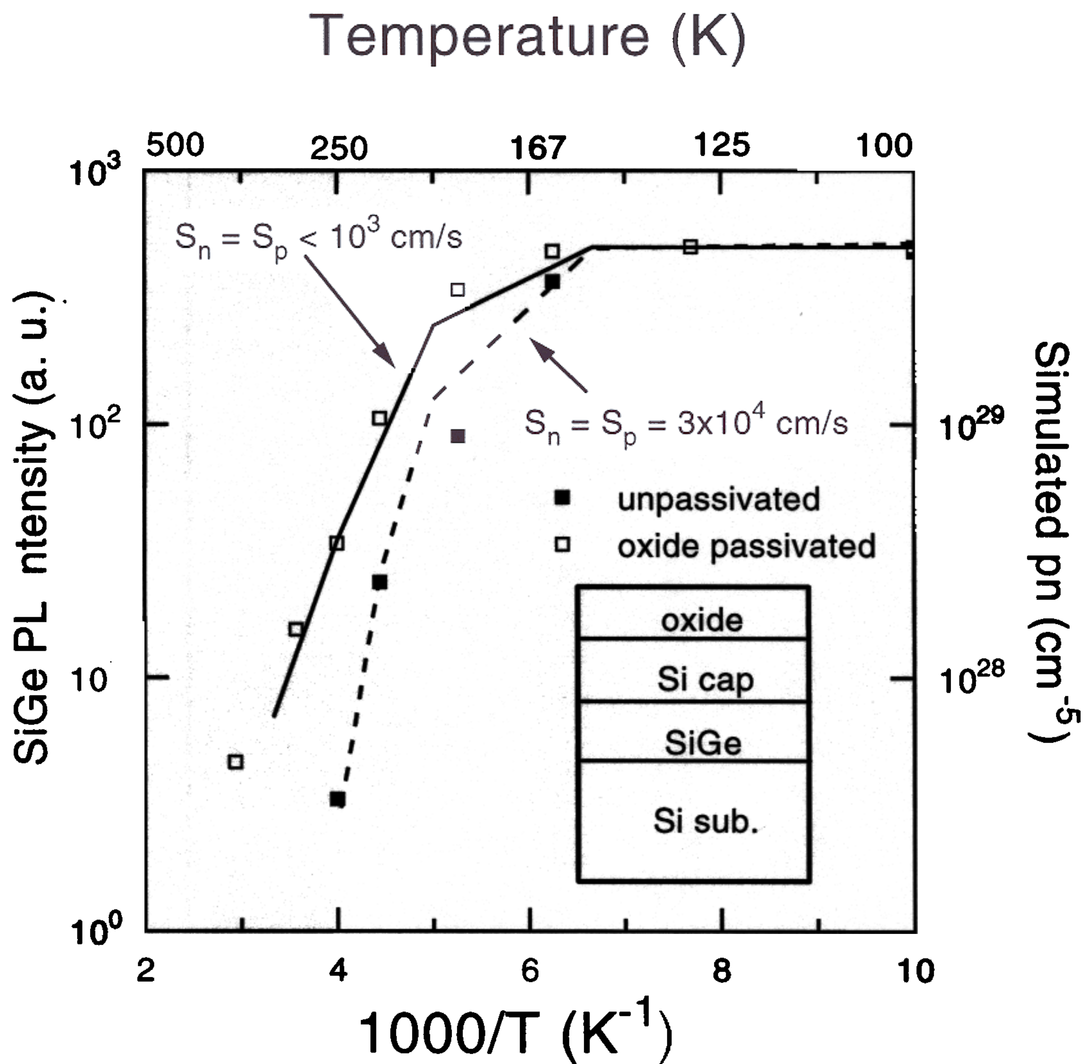

Figure 4.7: Measured integrated photoluminescence intensity and simulated pn as a function of inverse temperature. The squares are measured PL intensity, and the lines are simulated pn.

temperature luminescence intensity.

4.5 Pump Power Density Dependence

The photoluminescence pump power density was increased 100× from about 0.3 W/cm^2 to 30 W/cm^2, and the luminescence was re-measured from 77 to 300 K. At the higher power, the temperature dependence of the $Si_{1-x}Ge_x$ PL was qualitatively the same as at the lower power. At low temperature, the $Si_{1-x}Ge_x$ PL intensity was constant and was more than an order of magnitude stronger than the Si PL. Again at high temperature the $Si_{1-x}Ge_x$ PL rolled off as it had previously, but this time not until 250 K. The room temperature $Si_{1-x}Ge_x$ PL intensity was diminished only by a factor of two compared to its value at 77 K. Figure 4.9 compares the high and low pump power data for the oxide passivated sample #1623 (30% Ge). The relative intensities of these measurements were scaled by the measured pump power dependence at 77 K.

The analytical model was fit to the measured PL intensity, again keeping ΔE_G fixed at 210 meV. The best fit was for $\gamma = 3.9 \times 10^3$ (compared with 1.8×10^5 at low pump power density). The 46× decrease in γ and the associated higher temperature "knee" at higher pump power density can be phenomenologically explained by either an increased effective lifetime in the Si or a decreased lifetime in the $Si_{1-x}Ge_x$. An increased Si lifetime would preferentially enhance the high temperature $Si_{1-x}Ge_x$ PL by increasing the total effective lifetime (and therefore the carrier densities) at high temperature. Increasing the Si lifetime would have no effect at low temperature where the total effective lifetime is determined by recombination in the $Si_{1-x}Ge_x$, and thus it would increase the "knee" temperature. On the other hand, decreasing the $Si_{1-x}Ge_x$ lifetime would reduce the low temperature $Si_{1-x}Ge_x$ PL intensity, but not really affect that at high temperature when the electron and hole densities are

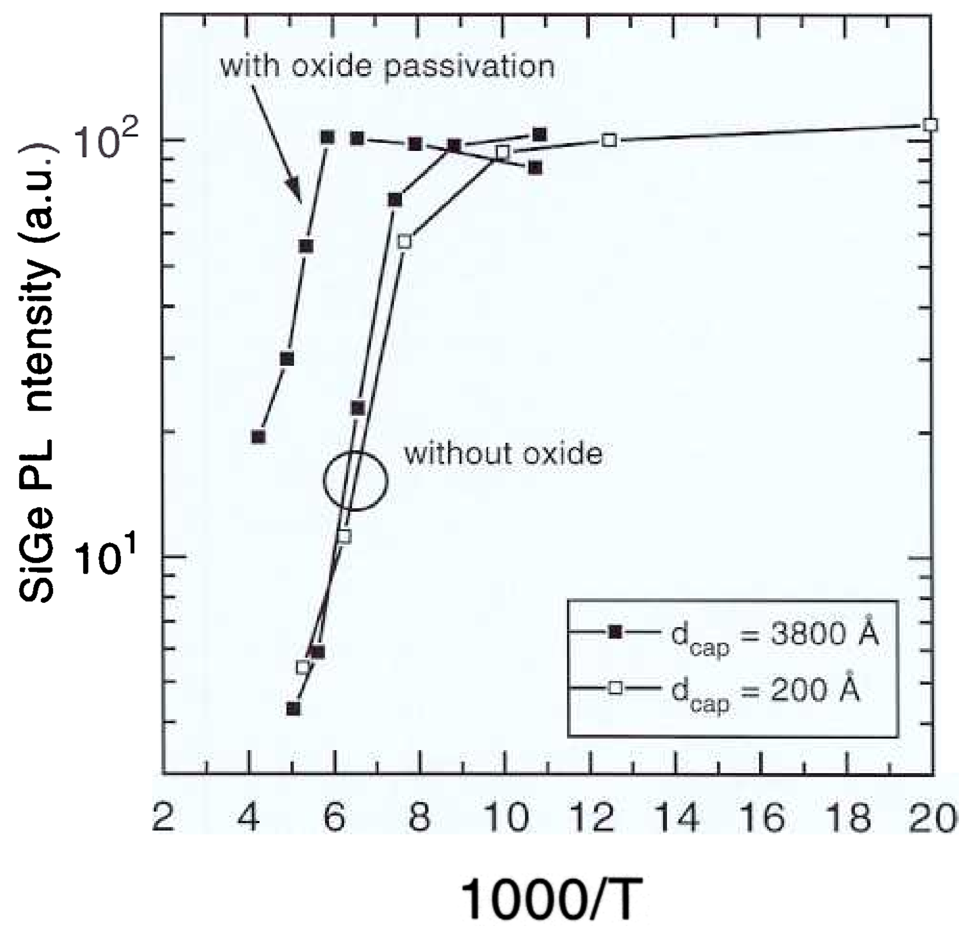

Figure 4.8: Temperature dependence of $Si_{0.8}Ge_{0.2}$ PL with thick and thin Si caps.

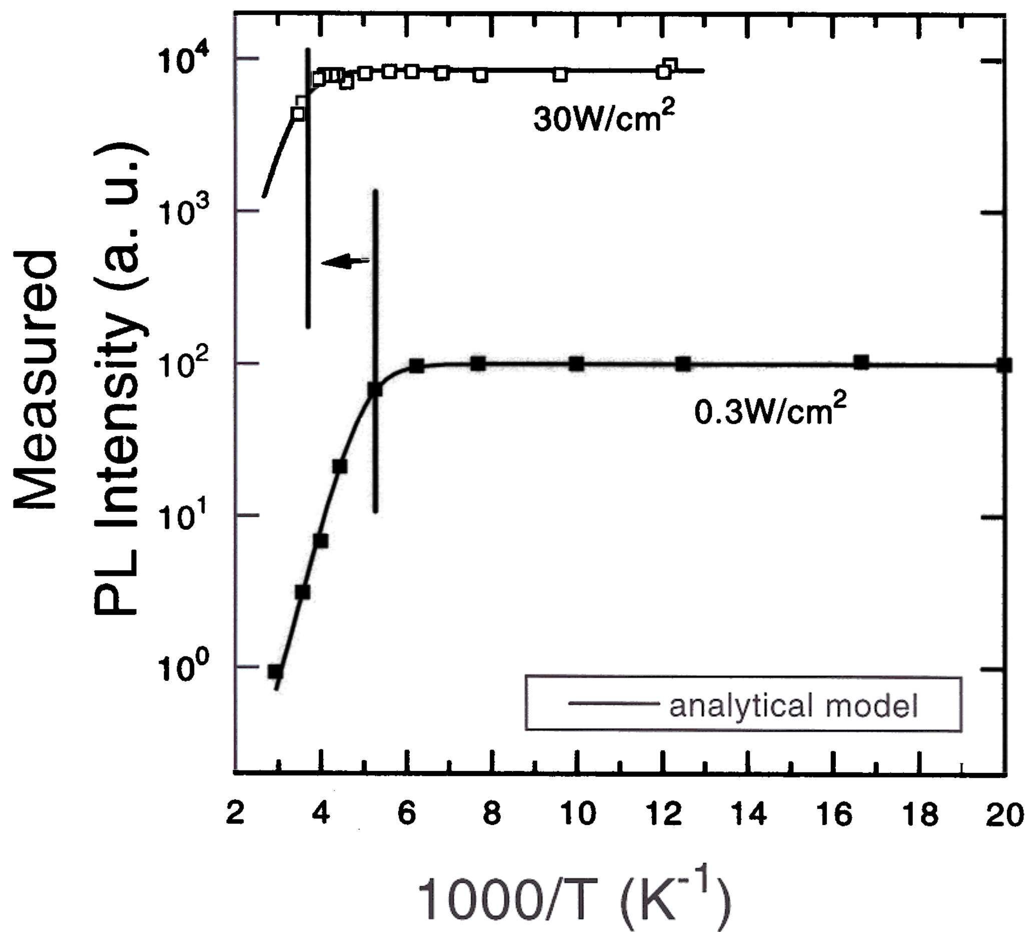

Figure 4.9: Temperature dependence of $Si_{0.7}Ge_{0.3}$ PL at high and low pump power density. The relative intensity was determined by measurement at 77 K.

determined by recombination in the Si.

Simulations were run at the higher pump power to sort out this behavior. It was found that Auger recombination plays a significant role in the $Si_{1-x}Ge_x$ at low temperature, especially at increased photogeneration rates. Under these conditions, the carrier densities in the $Si_{1-x}Ge_x$ are extremely high, approaching 10^{19} cm^{-3}. Auger recombination then dominates other processes and determines the effective lifetime and, consequently, the carrier densities and PL intensity. However, at higher temperatures, a significant number of carriers is thermally excited from the $Si_{1-x}Ge_x$ well, diminishing their density and the Auger recombination rate. The net result is a lower carrier concentration (and PL intensity) at low temperature with respect to at high temperature and, therefore, a higher "knee" temperature.

This effect can be understood by looking at the total effective lifetime defined in Chap. 3. Recall that τ_{eff} was defined as

$$\tau_{eff} = \frac{1}{P_{total}} \int \acute{n} \cdot dV \tag{4.7}$$

where P_{total} is the total photogeneration rate, $\acute{n}$ is the excess free electron density, and the integral is computed over the entire sample. We have plotted in Fig. 4.10 τ_{eff} as a function of inverse temperature for simulations at 0.3 and 30 W/cm^2. At the lower power, SHR recombination dominated because surface recombination was shut off by the oxide passivation, and the effective lifetime was essentially constant and equal to 1 μs. In contrast, at the higher power, the lifetime dropped to 0.1 μs at 150 K, while the room temperature lifetime remained at 1 μs. It was Auger recombination which killed the lifetime at low temperature and caused the high "knee" temperature at high pump power density.

Looking at Fig. 4.9, we see that the measured PL intensity increased almost exactly linearly with the pump power. One might then conclude that the total effective lifetime was constant and not a function of pump power. However, there is a subtle

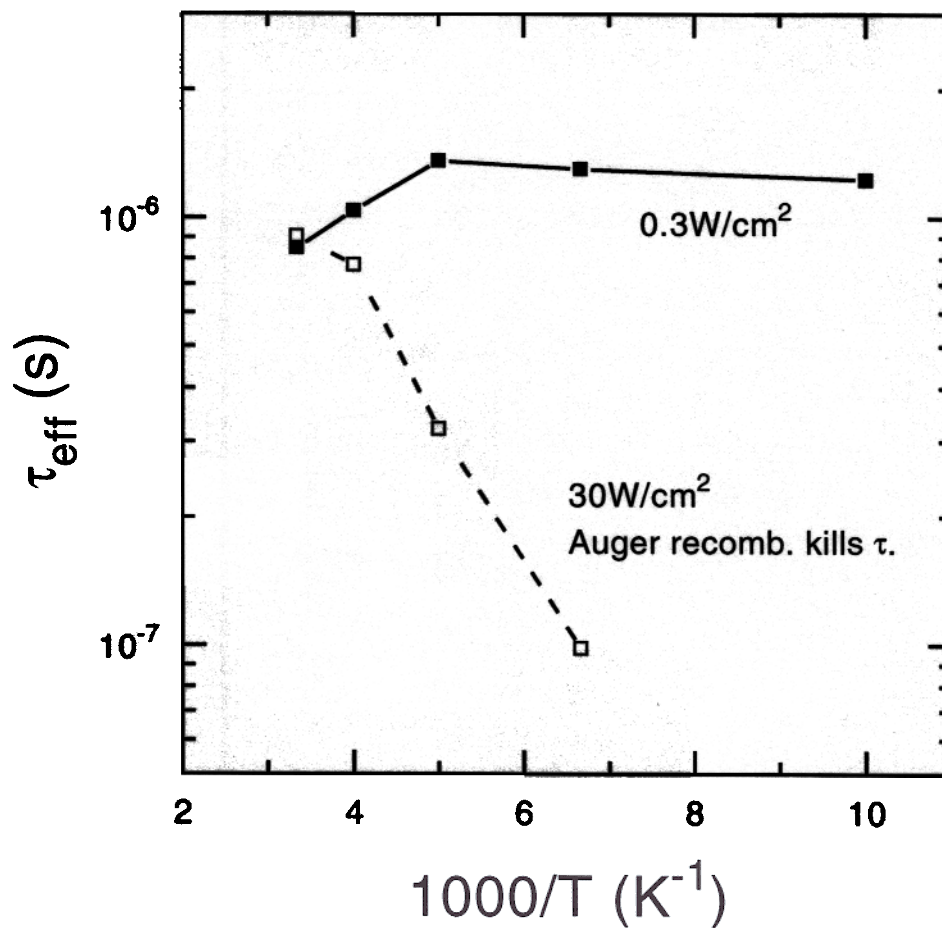

Figure 4.10: Comparison of the simulated total effective lifetime as a function of temperature at 0.3 and 30 W/cm^2.

point to consider. For the sake of a simple argument, take $n = p$ in the $Si_{1-x}Ge_x$, so that the PL intensity $I_{SiGe} \propto n^2$; and consider simplified SHR recombination ($R = n/\tau$). By definition, in steady-state, the pump rate P equals the total recombination rate R, and $I_{SiGe} \propto (R\tau)^2 \propto P^2$. Now for Auger recombination, $R \propto n^3$, so that $I_{SiGe} \propto P^{2/3}$. For all temperatures, the observed pump power dependence exhibited a power law between 2/3 and 2 and is consistent with a combination of SHR and Auger recombination.

4.6 Temperature Dependence of Electroluminescence

Several groups have measured electroluminescence (EL) from $Si_{1-x}Ge_x$ quantum well or Ge/Si superlattice light emitting diodes[43, 44, 35, 45, 46]. The available data has consistently shown that the EL intensity from such structures persists to higher temperature than does band-edge PL from similar structures, but no explanation had been offered for this phenomenon. We simulated temperature dependent EL in the structure of Mi *et al.* for which temperature dependent data was available[43, 47]. The simulated structure (Fig. 4.11) closely resembled the actual structure, with the only major difference being that the actual structure contained ten identical wells and our simulated structure contained just one. The single-well structure was chosen to ease comparison with the PL simulations, and our experience indicated that the number of wells does not significantly alter the results.

The temperature dependent EL data of Mi[47] is reproduced in Fig. 4.12 along with our temperature dependent PL data for the oxide passivated $Si_{1-x}Ge_x$/Si quantum well for comparison. In both cases, x = 0.30-0.35 and $d_{SiGe} \approx 50$ Å. Because the EL and the PL were measured in different set-ups by different researchers, the absolute intensities cannot be compared. Instead, the measured luminescence intensity in each case was scaled so that the low temperature EL/PL intensity ratio matched the

simulated ratio of the *pn* products. Notice that the EL intensity was roughly uniform from 100 to 300 K, while the PL intensity characteristically rolled off at high temperature. The behavior was well reproduced by the simulated *pn* product, and two factors contributing to the flatter EL temperature dependence were identified. First, these EL simulations, matching the actual measurement conditions, were performed at a drive current density of 280 A/cm^2, corresponding to a pump rate 4000$\times$ higher than that during the PL measurements. Second, the n^+ buried contact layer blocks hole transport to the substrate, effectively shrinking the device structure.

The typically much higher pump rates during EL experiments result in higher electron and hole densities in the $Si_{1-x}Ge_x$ quantum wells of those structures. However, in our simulation, the low temperature *pn* product increased only by a factor of 200 compared to the PL, while the pump rate had increased 4000 fold. This disparity between the increase in the pump rate and the increase in the carrier density corresponds to a reduction of the total effective lifetime τ_{eff} in the sample. Recall that at low temperature, τ_{eff} is determined by the $Si_{1-x}Ge_x$, because most of the carriers are trapped there. As we saw with the PL at high pump power density, Auger recombination flattens the temperature dependence by suppressing the carrier densities at low temperature. To render a fair comparison between PL and EL temperature dependence, EL simulations (67 mA/cm^2) were performed at the same total injection rate (4×10^{17} cm^{-2}/s) as the low power PL simulations (0.3 W/cm^2). These simulation results are compared to the PL simulations in Fig. 4.13. As expected, the low temperature *pn* products were identical, and the EL "knee" was now at much lower temperature than it was at high drive current. The EL "knee" did however remain at a higher temperature than did the PL "knee," implying a second factor contributing to the higher temperature "knee" in EL experiments.

At higher temperatures, the carriers in $Si_{1-x}Ge_x$ are in equilibrium with their respective populations in the Si substrate and cap. Thus, the relative carrier *densities*

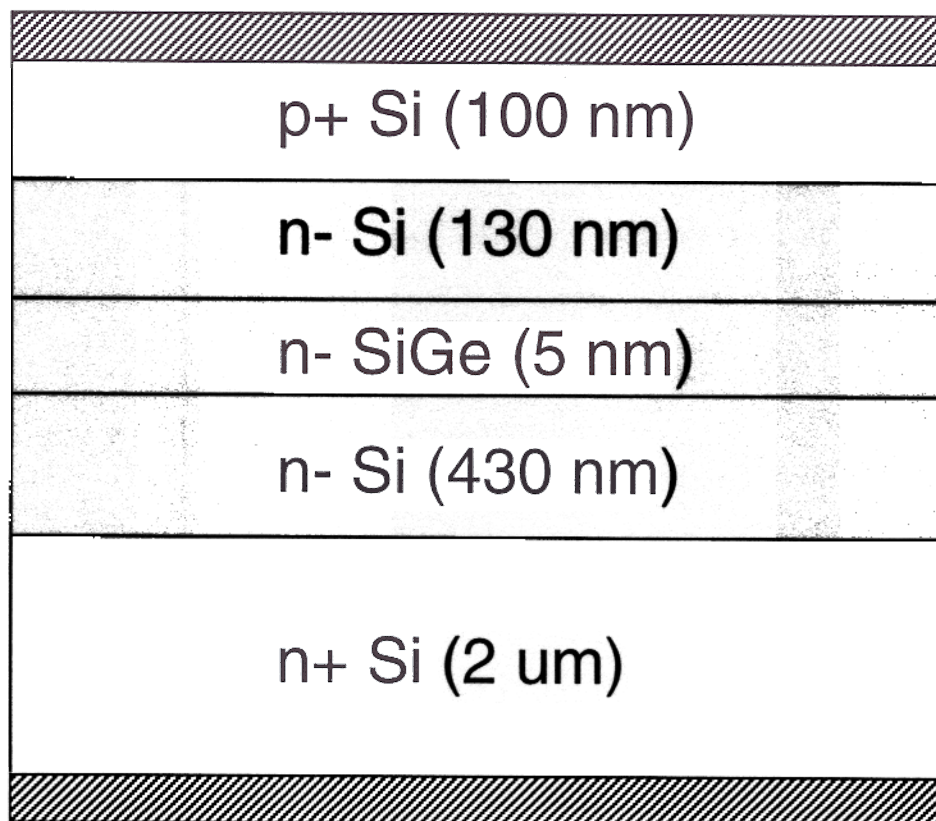

Figure 4.11: Simulated EL structure.

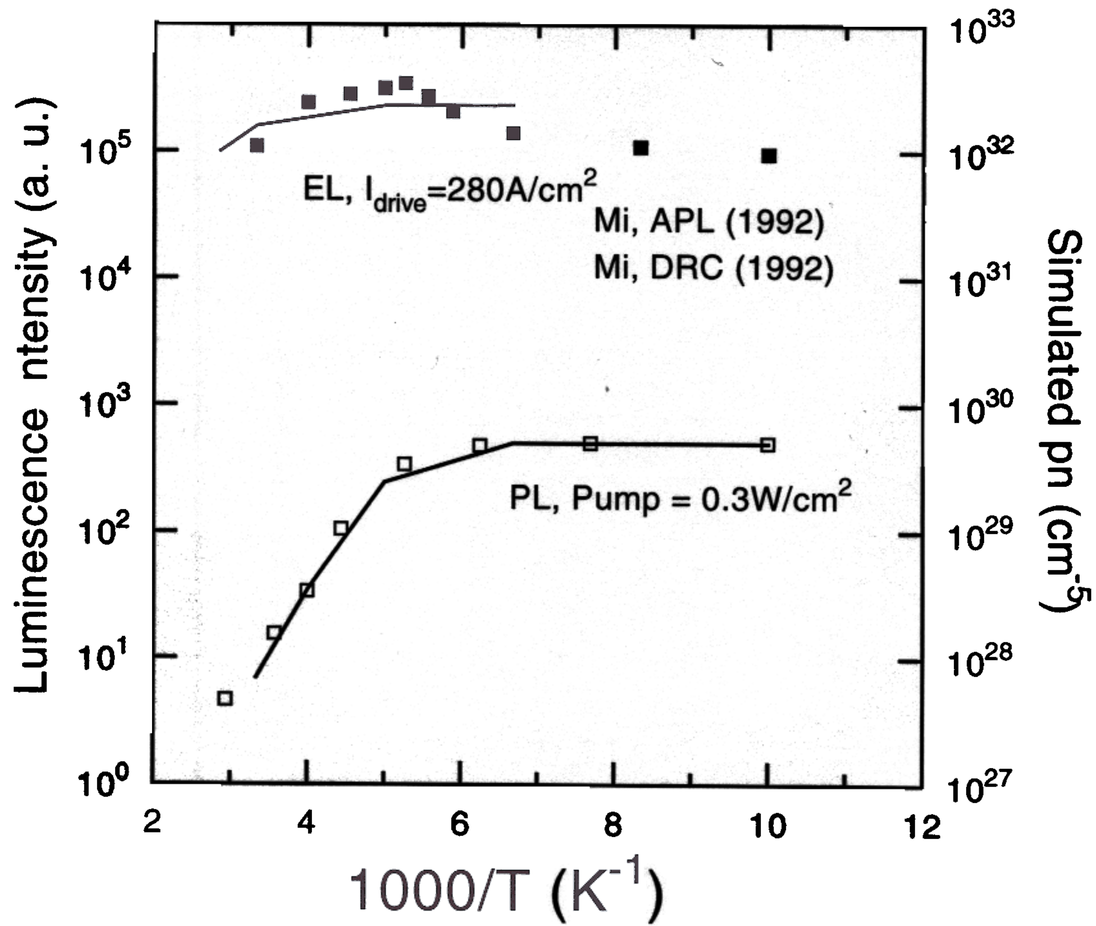

Figure 4.12: Measured PL and EL intensity and simulated integrated pn in $Si_{1-x}Ge_x$ as a function of inverse temperature. The EL data was taken from the work of Mi *et al.*[47]. The squares are measured intensity, and the lines are simulated pn.

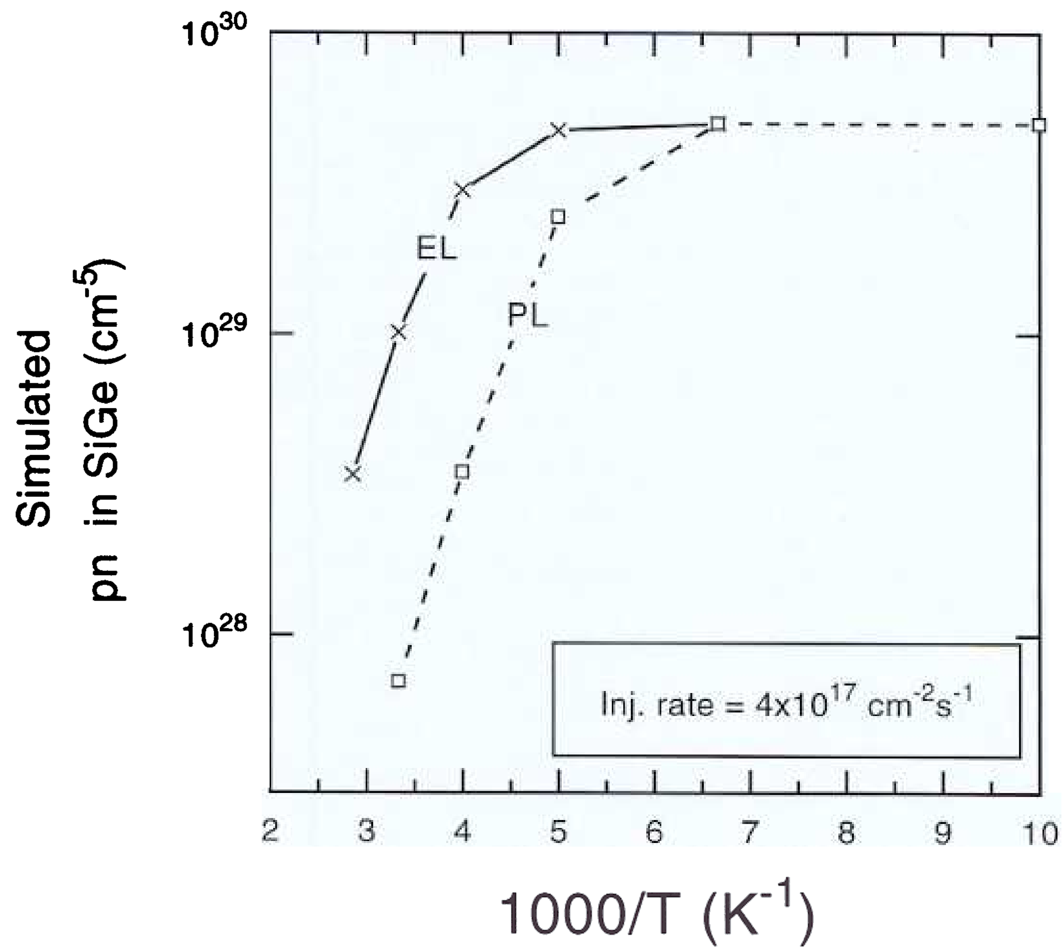

Figure 4.13: Simulated pn product in $Si_{1-x}Ge_x$ as a function of inverse temperature. The injection rate for both PL and EL was $4 \times 10^{17} cm^{-2}/s$

are determined solely by quasi-equilibrium. However, the *total* number of carriers in the Si compared to in the $Si_{1-x}Ge_x$ and, therefore, the luminescence intensity, depends on the effective widths of each region. The effective $Si_{1-x}Ge_x$ width is trivially just the width of the layer, or the sum of the layer widths in a multiple quantum well structure.

The effective Si width is more difficult to nail down. In a PL experiment, $W_{Si,eff}$ has a lower bound of the absorption depth of the pump (1 μm) and an upper bound of the substrate thickness (500 μm). $W_{Si,eff}$ is the width of the region over which the carriers distribute themselves, on the order of the minority carrier diffusion length; and since it is determined by thermal diffusion and lifetime, it is a function of temperature. For example, at 250 K significant photogenerated minority carriers were found by simulation as deep as 100 μm into the substrate, using $\tau_{SHR} = 1$ μs. In comparison, $L = \sqrt{D\tau} = 50$ μm. In our EL simulations, holes injected from the top p^+ contact traversed the undoped region with many getting collected in the $Si_{1-x}Ge_x$ well. Those that did reach the n^+ layer immediately recombined so that essentially no holes escaped the i-layer. The effective Si width then, in this case, equals the i-layer thickness. See Fig. 4.14. Going back to the analytical model, we see that a small $W_{Si,eff}$ means a small γ and consequently a high "knee" temperature.

Additional simulations were performed with an increased i-layer thickness to confirm that indeed it played a role in the EL temperature dependence. Fig. 4.15 shows integrated *pn* as a function of inverse temperature for EL simulations with two i-layer thicknesses (0.6 and 1.6 μm) and for the PL simulation. All were performed at the same total injection rate, resulting in equal *pn* up to 150 K. However, the "knee" of each is clearly inversely related to $W_{Si,eff}$; as $W_{Si,eff}$ was increased, the high temperature *pn* in $Si_{1-x}Ge_x$ decreased.

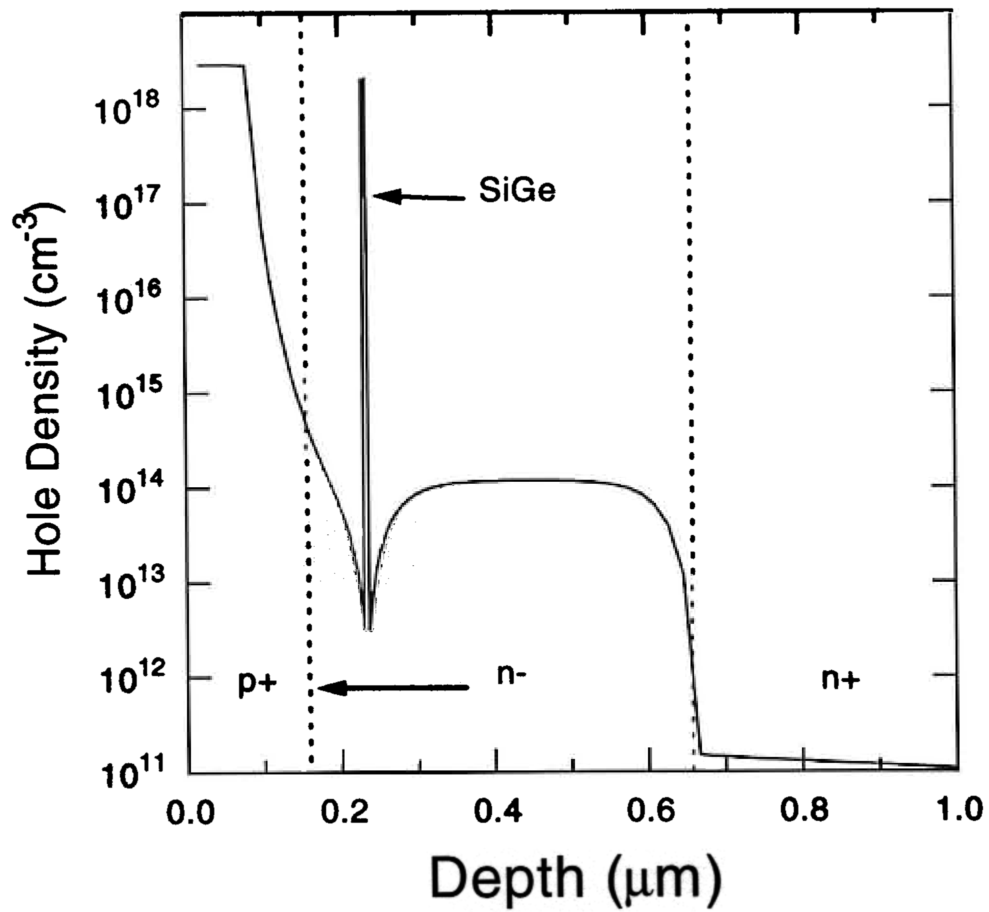

Figure 4.14: Simulated hole density at 200 K for a drive current of 67 mA/cm^2.

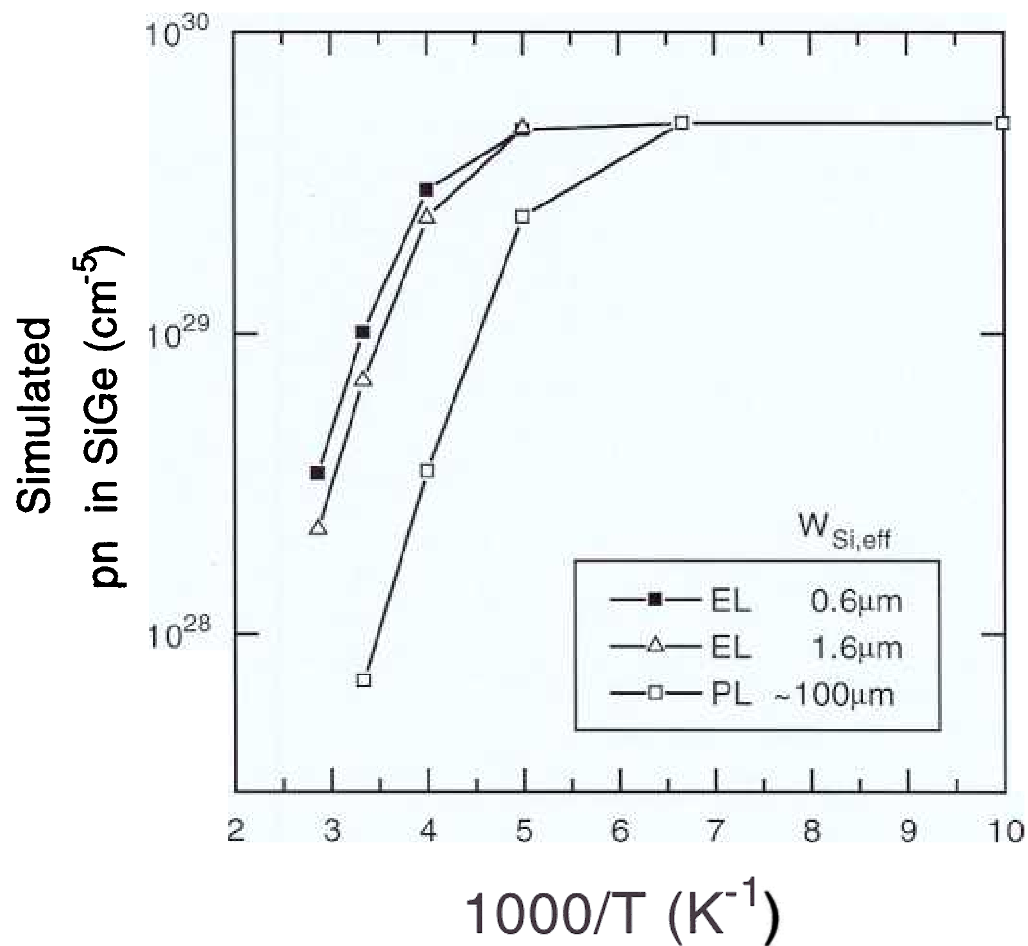

Figure 4.15: Simulated integrated *pn* in $Si_{1-x}Ge_x$ as a function of inverse temperature. The total injection rate was the same in all cases.

4.7 Summary

In this chapter, we saw that the photoluminescence intensity in strained $Si_{1-x}Ge_x$/Si heterostructures at high temperatures is controlled by recombination at the top Si surface, rather than by a property of the $Si_{1-x}Ge_x$ itself. Furthermore, the room temperature photoluminescence intensity can be increased dramatically by passivating the top surface with thermal oxide, and this behavior was well reproduced by numerical simulation coupled to a luminescence model. Based on further numerical simulation, two mechanisms were identified as the origin of the difference in temperature dependence between photo- and electroluminescence. First, at high current density Auger recombination in the $Si_{1-x}Ge_x$ reduces the luminescence intensity at low temperature. Second, the heavily doped buried contact layer in *p-i-n* diodes blocks the transport of minority carriers to the substrate.

Chapter 5

Pseudomorphic $Si_{1-x-y}Ge_xC_y$ Alloys on Si (001)

5.1 Introduction

The lattice parameter of Ge is 4.2% larger than that of Si. We saw in Chap. 2 that this misfit causes biaxial compressive strain in commensurate $Si_{1-x}Ge_x$ films on Si substrates. Associated with this strain is a finite critical thickness, which constrains the design and processing of strained $Si_{1-x}Ge_x$ heterostructures. The lattice parameter of diamond, however, is smaller than that of both Si and Ge. Commensurate $Si_{1-y}C_y$ films are under tension[48] and can be exploited for their large conduction band offset to Si[49, 50], which is lacking in compressively strained $Si_{1-x}Ge_x$. Furthermore, in principle, a $Si_{1-x-y}Ge_xC_y$ alloy[51, 52] with the proper composition will be lattice matched to Si and, therefore, be strain-free. These new materials, tensilely strained $Si_{1-y}C_y$ and reduced-strain $Si_{1-x-y}Ge_xC_y$, offer the potential for many new Si-based heterostructures, including n-type MODFETs without the use of relaxed buffers and single heterojunction bipolar transistors.

This chapter begins with some relevant background material concerning the properties of C in Si and some techniques for measuring the C content of Si We then discuss significant previous work on $Si_{1-y}C_y$ and $Si_{1-x-y}Ge_xC_y$ alloys before describing our growth (by Rapid Thermal Chemical Vapor Deposition) and structural characterization of $Si_{1-x-y}Ge_xC_y$ thin films on Si (001). The opto-electronic properties of

films are treated in the following chapter.

Carbon in Silicon

5.2.1 Solid solubility and diffusion

Carbon contamination exists in all forms of Si. Bulk Si formed by the Czochralski (Cz) pulling technique typically contains C levels close to 10^{16} cm^{-3}[53], and although very low C content substrates can be fabricated by the ultra-clean float zone (FZ) method, many FZ wafers still contain carbon concentrations $\sim 10^{16}$ cm^{-3}, due to the starting material[54]. Because of its ubiquity, the behavior of carbon in Si has received intense scrutiny, and good review papers[54] are available. A comprehensive review will not be attempted here, but for completeness, a few important points will be addressed.

First of all, at low concentrations, C in Si is completely benign. It is almost exclusively a random substitutional impurity; and because it shares a valence of four with Si, it is not electrically active. However, in contrast to Si and Ge which are completely miscible, the solid solubility of substitutional carbon C_s is quite low, only about 4×10^{17}cm^{-3} near the melting point of Si[55, 56]. (See Fig. 5.1.) Above the solid solubility, the stable form of C in Si is no longer a random alloy but the ordered compound SiC. But the removal of C from solution and to SiC precipitates is difficult in oxygen-free Si[57] due in part to the slow diffusion of C_s. The diffusion constant of substitutional C[58, 59] is plotted as a function of inverse temperature on Fig. 5.1.

The behavior of C in Si becomes decidedly more complex and troublesome when in the presence of other point defects, such as self-interstitials, oxygen interstitials, and dopants. Si self-interstials combine with C_s to form interstitial carbon C_i. Actually, the C_i consist of a C and Si atom sharing a single atomic site as a "split interstial." These diffuse very rapidly above room temperature[60] (Fig. 5.1). The C_i are not only

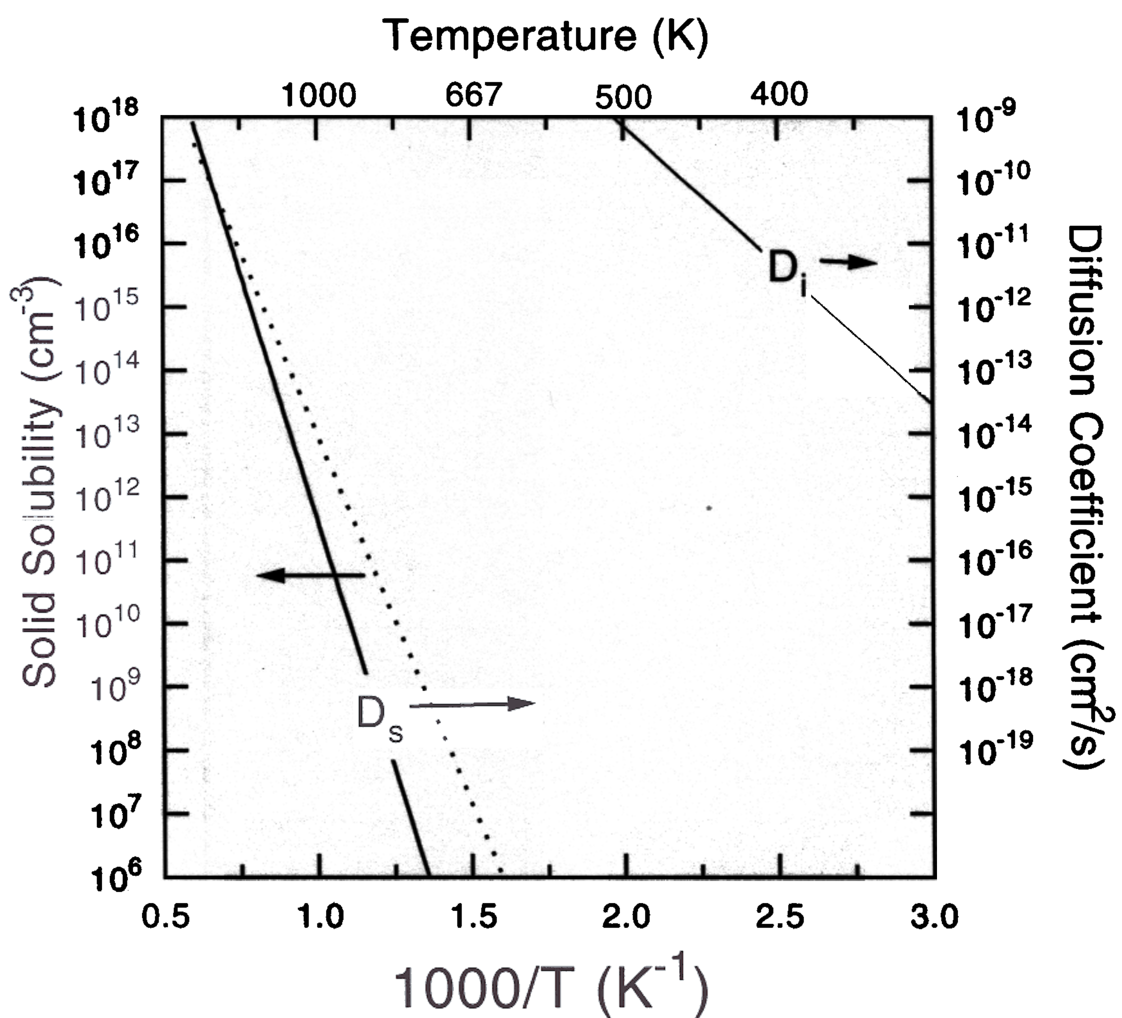

Figure 5.1: Solid solubility of C in Si (dotted line)[55] and the diffusion coefficients of C_s[59] and C_i[60] in Si as a function of inverse temperature.

highly mobile but also form a large number of poorly characterized complexes with many other impurites, producing electrically active defect centers of varying thermal stability[54]. Unfortunately, Si self-interstials are produced by some of the most common Si processing techniques, including thermal oxidation, ion implantation, and in-diffusion of phosphorus.

The mutual presence of oxygen and carbon in Si is well known to aid the precipitation of both SiO_x and SiC[54, 57]. The formation of SiO_x by precipitation from interstitial oxygen O_i creates a local volume expansion which must be accommodated by the removal of a Si atom, usually by the diffusion of self-interstitials from the precipitate. Conversely, to prevent local volume reduction and void formation, SiC precipitation injects almost one vacancy per C_s atom. Thus, the simultaneous precipitation of O_i to SiO_x and C_s to β-SiC is energetically favored in that it results in no net volume change. Such co-precipitation has been verified by annealling experiments which showed that there is a net reduction in both $[O_i]$ and $[C_s]$ and that $\frac{d[O_i]}{dt} \sim 2\frac{d[C_s]}{dt}$[61].

The above discussion of C solubility in Si, strictly speaking, is completely true only for bulk samples. The problem of SiC precipitation might be somewhat mitigated by two aspects of epitaxial growth. First, during the growth process, the bulk solubility of C is not really relevant. Rather, a "surface solubility" determines the incorporable substitutional C content[62]. Due to the additional degrees of freedom to relax atomic positions at and near the surface, the surface solubility of some atoms can be orders of magnitude larger than their bulk solubility. Secondly, it has been previously observed that epitaxial semiconductor structures not found in the bulk can be stabilized by substrate-imposed strain. Calculations by Rücker *et al.*[63] indicate that $Si_{1-y}C_y$ structures containing up to 20% C which avoid nearest-neighbor and next-nearest-neighbor C-C pairs can be "strain-stabilized."

5.2.2 Measuring substitutional carbon

Substitutional C in Si has a room temperature local vibrational mode at 605 cm^{-1}. The oscillator strength of this mode has been measured so that the absorption coefficient α at 605 cm^{-1} may be used as a measure of $[C_s]$.

$$[C_s] = \gamma\alpha \tag{5.1}$$

where the "constant" $\gamma = 1.1 \pm 0.2 \times 10^{17}$ cm^{-2}[54] for α in units of cm^{-1}. The uncertainties in calibration arise from difficulties in independently determining $[C_{total}]$ and $[C_s]$. This technique has the advantage of being non-destructive and of being able to differentiate between C_s, C_i (922 and 932 cm^{-1}), and SiC. However, there are difficulties in detecting substitutional C by IR absorption. First, recall that Si substrates contain substitutional C. For example, a 0.5 mm thick Si wafer with $[C_s] = 10^{16}$ cm^{-3} has an areal C density of 5×10^{14} cm^{-2}. Our $Si_{1-x-y}Ge_xC_y$ films had typical thicknesses and C contents of 100 Å and 1%, yielding an areal density of 5×10^{14} cm^{-2} so that at best $[C_{total}]$ in our films was roughly equal to the amount already in the substrate. This problem could be solved through the use of low C content FZ substrates or by subtracting the absorption spectrum of an identical reference substrate. Additionally, there is IR absorption near 605 cm^{-1} in intrinsic Si due to the emission of two phonons[64]. This problem can only be solved by subtracting the spectrum of a reference substrate of equal thickness.

The lattice spacing of C-doped Si is smaller than that of pure Si. X-ray measurements by Baker *et al.*[65] showed that the changes in lattice constant were within 10% of those expected from Vegard's law. Therefore, measurement of the lattice spacing then can be used with Vegard's law to determine $[C_s]$. This technique can be extended to strained $Si_{1-x-y}Ge_xC_y$ alloys, using equations analogous to those in Chap. 2. Now the vertical lattice constant, as measured by X-ray diffraction (XRD), is a function of Ge fraction (x) and C fraction (y). For $Si_{1-x-y}Ge_xC_y$ interpolating between Si, Ge,

and diamond indicates that $x/y = 8.3$ yields a film lattice-matched to Si, whereas experimental values obtained by different authors vary from 8 to 10[52, 66, 67]. Most likely the differences are due to the difficulties as discussed above in accurately measuring $[C_{total}]$ and $[C_s]$. For this thesis, we have assumed the ideal value of 8.3. For example, a film containing 20% Ge and 1% C will have an XRD spectrum very similar to that of a film with 12% Ge and no C, if both films are fully strained. So, this technique for measuring [C] requires no standards but does demand knowledge of the Ge content and the strain condition of the film, and it assumes all of the C is substitutional.

Other common methods of elemental analysis are available but are not completely satisfactory. Secondary Ion Mass Spectroscopy (SIMS) requires calibration with many known standards to account for possible "matrix effects" and is notoriously inexact. Auger Electron Spectroscopy (AES) also requires standards and, worse yet, does not have the necessary sensitivity (~1 atomic %). Also, these techniques do not distinguish between the various forms of C: substitutional, interstitial, and SiC. Rutherford Back-scattering Spectroscopy (RBS) generally requires that the trace elements being detected be heavier than the substrate elements. This is the case for Ge, but not C, on Si. However, utilization of an elastic C resonance $^{12}C(\alpha, \alpha)^{12}C$ reaction which enhances the C signal ~100-fold has been used to quantify C contents as low as 0.5% in 1100 Å $Si_{1-x-y}Ge_xC_y$ films[68], but our interest is in thinner films with sometimes lower C levels.

5.3 Previous Work

Pseudomorphic $Si_{1-y}C_y$ and $Si_{1-x-y}Ge_xC_y$ alloys have been formed by several groups using a wide variety of growth techniques, including solid phase epitaxy,[69, 70] molecular beam epitaxy (MBE),[48, 51, 71] plasma-enhanced chemical vapor deposition

(PE-CVD),[72] and thermal CVD[52, 67, 73]. Most of this work has been of a structural nature, with reports of strain as a function of C content for example. All have shown that indeed incorporating substitutional C into either Si or $Si_{1-x}Ge_x$ adds tensile strain in a predictable manner. The consensus derived from this body of work is that, for small y, the lattice parameter of these alloys is roughly linear in y, as we saw in Chap. 2 that it was in x. There is further agreement that higher growth temperatures and higher C contents tend to favor SiC precipitation, but the exact conditions of this transition depend on factors such as growth rate.

Reports on the optical and electrical properties of $Si_{1-y}C_y$ and $Si_{1-x-y}Ge_xC_y$ have been fewer, but there too some consistency has emerged: the electronic band structure can not be modeled merely as an interpolation between those of Si, Ge, and C[74, 73, 50]. The incorporation of substitutional C affects the band structure of pseudomorphic films in two ways: (1) by reducing the average lattice constant, C gives rise to a macroscopic strain field which shifts the bands; (2) the C atoms themselves represent local fluctuations in the crystal potential. The first effect may be computed within the framework of deformation potentials as discussed in Chap. 2, provided that the elastic constants and deformation potentials are known or assumed. The second effect, that of the C atoms themselves, is less straightforward; however, the picture is becoming more clear. It will be seen in more detail in the next chapter that our PL results on $Si_{1-x-y}Ge_xC_y$[73] indicate that C *reduces* the fundamental band gap of *relaxed* $Si_{1-x-y}Ge_xC_y$ despite the large band gaps of diamond and SiC. Our results in $Si_{1-x-y}Ge_xC_y$ show that C has the same intrinsic effect on the band gap of $Si_{1-x}Ge_x$ as Brunner *et al.*[50] showed in $Si_{1-y}C_y$ that it does on the band gap of Si.

5.4 Rapid Thermal CVD of $Si_{1-x-y}Ge_xC_y$

In 1993, Regolini *et al.*[52] first demonstrated the use of Rapid Thermal Chemical Vapor Deposition (RTCVD) for the formation of $Si_{1-x-y}Ge_xC_y$ films on Si substrates. Their initial films were grown at 650°C using hydrogen-diluted germane, dichlorosilane (DCS), and either tetraethylsilane or tetramethylsilane as the C source. These single crystal films contained 0.6-0.7 atomic % C and demonstrated partial strain compensation compared to C-free films. Subsequent work by the same group demonstrated band-edge photoluminescence (although accompanied by defect lines) from films containing up to 0.9% C. Mi *et al.*[67] investigated the use of methylsilane as a carbon precursor. Their results at 550-600°C using silane and germane showed a very high C incorporation efficiency for $y < 0.02$, but the C content tended to saturate near 2.2% independent of the Ge fraction

Our $Si_{1-x-y}Ge_xC_y$ films were grown by RTCVD using dichlorosilane (DCS), germane (0.8% in H_2), and methylsilane (1% in H_2) as precursors with H_2 as a carrier gas[75, 76, 77]. The growth pressure was always 6 torr, and the growth temperature was varied from 550 to 625°C. The DCS flow was kept constant at 26 sccm, while the germane and methylsilane flows were adjusted to vary the composition of the films. Fig. 5.2 shows X-ray diffraction (XRD) spectra from two sets of samples, one grown at 575°C and the other at 625°C. In all cases, the DCS and germane flows were 26 and 0.8 sccm, respectively. The methylsilane flow was varied from 0 to 0.2 sccm to adjust the C concentration of the films. The $Si_{1-x-y}Ge_xC_y$ films were under biaxial compressive strain so that their in-plane lattice constant matched that of the Si substrate, while their lattice spacing in the growth direction was greater than a_{Si}. Therefore, the $Si_{1-x-y}Ge_xC_y$ (400) XRD peaks appeared at smaller angle than did the Si peak ($2\theta = 69.1°$). The position of the $Si_{1-x-y}Ge_xC_y$ signal shifted towards the Si signal as the methylsilane flow, and consequently $[C_s]$, was increased, indicating a

reduction in misfit strain.

The Si substrate was represented by two peaks because the X-ray source contained both Cu $K_{\alpha 1}$ and $K_{\alpha 2}$ radiation. Due to spectral broadening, these two lines could not be resolved in the $Si_{1-x-y}Ge_xC_y$ spectra, resulting in an estimated uncertainty in the strain of ± 0.0004. According to the Scherrer formula[78], the XRD linewidth from a thin film is inversely proportional to its thickness. For our 400-600 Å $Si_{1-x-y}Ge_xC_y$ films, the Scherrer broadening yields a FWHM of $\sim 0.19°$ 2θ. Additionally, the lines suffered from instrument broadening, as seen in the Si substrate peaks which had FWHM=0.10°. The sum of the Scherrer broadening and the instrument broadening equalled the width of the unresolved $Si_{1-x-y}Ge_xC_y$ Cu $K\alpha 1$ and $K\alpha 2$ peaks.

Assuming that adding C did not significantly alter the Ge fraction, the magnitude of the shift away from the $y = 0$ sample was converted into the C fraction. Again, this was done assuming that 1% C compensates the strain induced by 8.3% Ge. The substitutional C fraction for both conditions, 575°C and 625°C, is plotted as a function methylsilane flow in Fig. 5.3. Note first that, all other conditions being equal, the C fraction was higher for the lower growth temperature and growth rate (12 Å/min vs. 80 Å/min). At 625°C, the C fraction saturated near 1.2%. For growth under similar circumstances, Bodnar and Regolini[79] showed that $[C_s]$ measured by XRD and FTIR saturated at high methylsilane flow while $[C_{total}]$ measured by SIMS did not, indicating that the assumption that all C atoms are substitutional breaks down under some conditions. However, the data of Mi[67] showed both the SIMS-measured $[C_{total}]$ and the strain compensation saturating together. This whole issue of $[C_s]$ and $[C_i]$ vs. $[C_{total}]$ is critical and remains unresolved.

Some of our samples were analyzed by SIMS by Dr. Charles Magee of Evans East. Despite attempts to calibrate using $Si_{1-x}Ge_x$ samples implanted with a known dose of C, $[C_{total}]$ as measured by SIMS was consistently *lower* than $[C_s]$ measured by XRD, opposite to what would be expected if some C was not substitutional. We associate

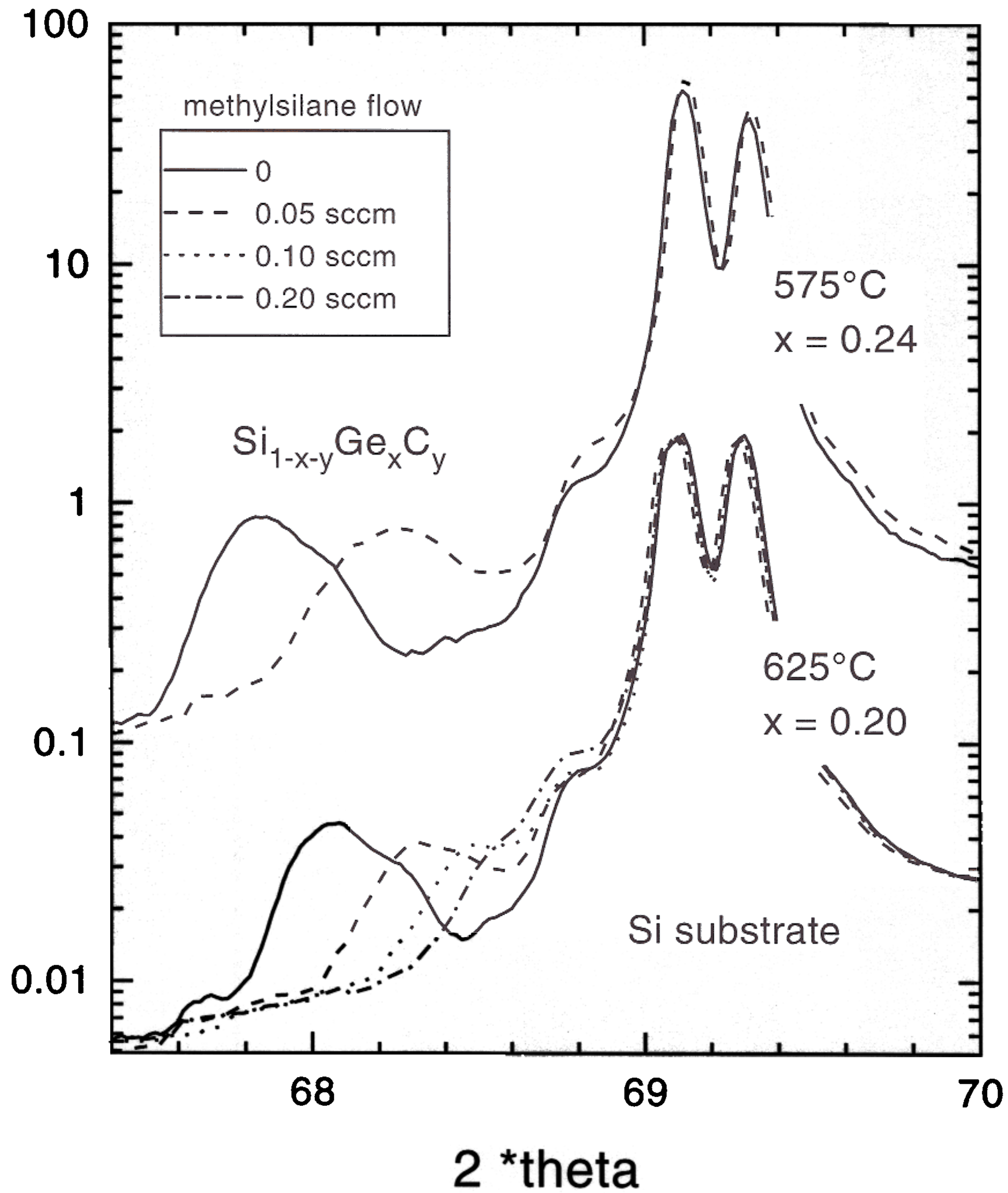

Figure 5.2: X-ray diffraction spectra for $Si_{1-x-y}Ge_xC_y$ thin films on Si (001). The Si substrate signal was a doublet because the X-ray monochromator could not resolve Cu $K_{\alpha 1}$ and $K_{\alpha 2}$. The $Si_{1-x-y}Ge_xC_y$ signal was weaker and broader than the Si substrate signal because the films were quite thin (400-600 Å).

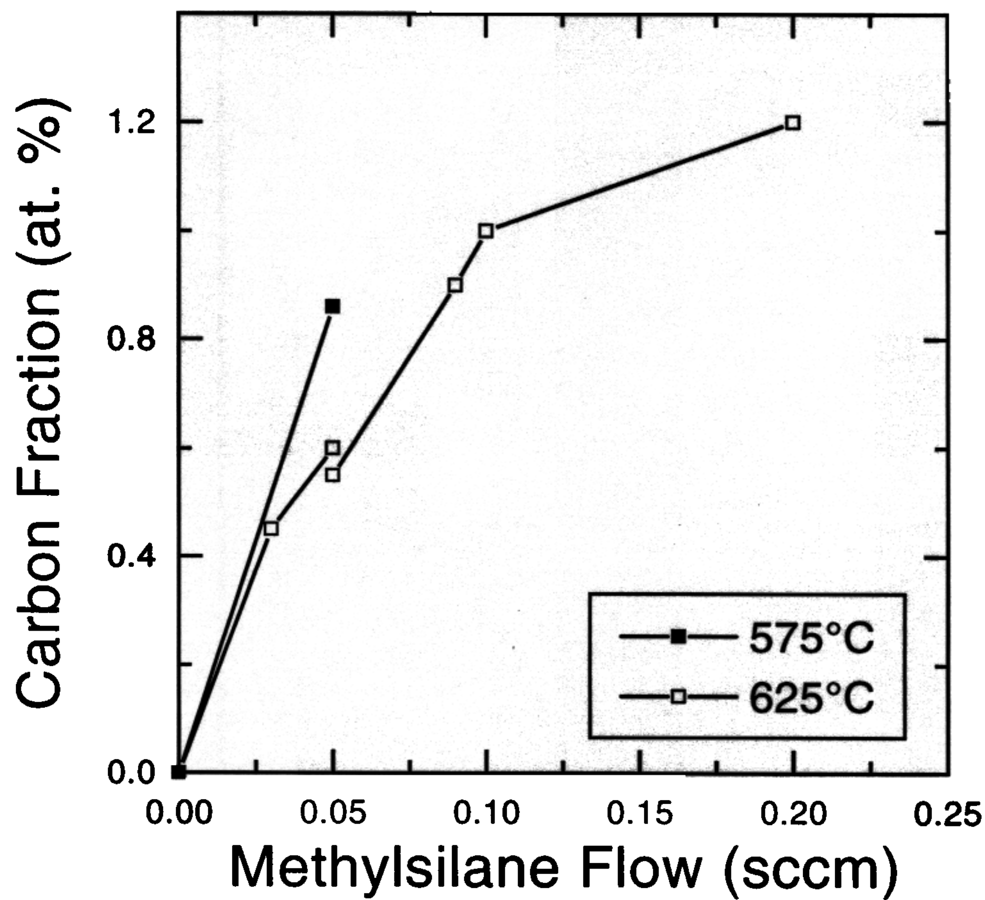

Figure 5.3: C fraction measured by XRD as a function of methylsilane flow. The Ge fractions were 0.20 and 0.24 for growth at 625 and 575°C, respectively.

the inconsistency between SIMS and XRD with poor SIMS calibration. However, the SIMS analysis did show that the C had a box-like profile with sharp interfaces. See Fig. 5.4. The slope of the top interface of the C profile was ~50 Å/decade. Taking this as an upper limit to the diffusion length L_D, for a 10 minute Si cap growth at 675°C we get a diffusion coefficient $D = 4 \times 10^{-16}$ cm^2/s, very close to the value for substitutional C (see Fig. 5.1). Recalling that interstitial C diffuses very rapidly above room temperature, the small amount of measured diffusion was indirect evidence that the C was substitutional rather than interstitial.

The SIMS also confirmed Mi's result that there was no detectable variation of Ge content as methylsilane was added to the gas mixture. Moreover, we observed only a slight variation in growth rate as a function of C content. Fig. 5.5 shows the growth rate of several $Si_{1-x-y}Ge_xC_y$ films measured by SIMS. For x 0.38, there was a small growth rate reduction (~-20% for 1% C); while for $x = 0.24$, there was no measured change in growth rate. Constant growth rates are consistent with a constant Ge fraction in that the growth rate increases sharply with x.

5.5 Summary

Traditionally, the problem of C in Si has been solved by reducing the C level below the point where it is significant (i.e., ~10^{16} cm^{-3}). However, now we wish to dope Si and $Si_{1-x}Ge_x$ with as much as several percent of C. Techniques, predominantly MBE and low temperature CVD, have been developed for forming such C alloys with ~2% or less substitutional C. Two major areas of concern remain. First, what controls the position of the C atoms in the lattice? Are they substitutional, interstitial, or precipitated as SiC? And what process conditions yield each of these forms? Second, what are the effects of C, particularly substitutional, on the opto-electronic properties of $Si_{1-y}C_y$ and $Si_{1-x-y}Ge_xC_y$ alloys? The final chapter of this thesis addresses some parts of this second question.

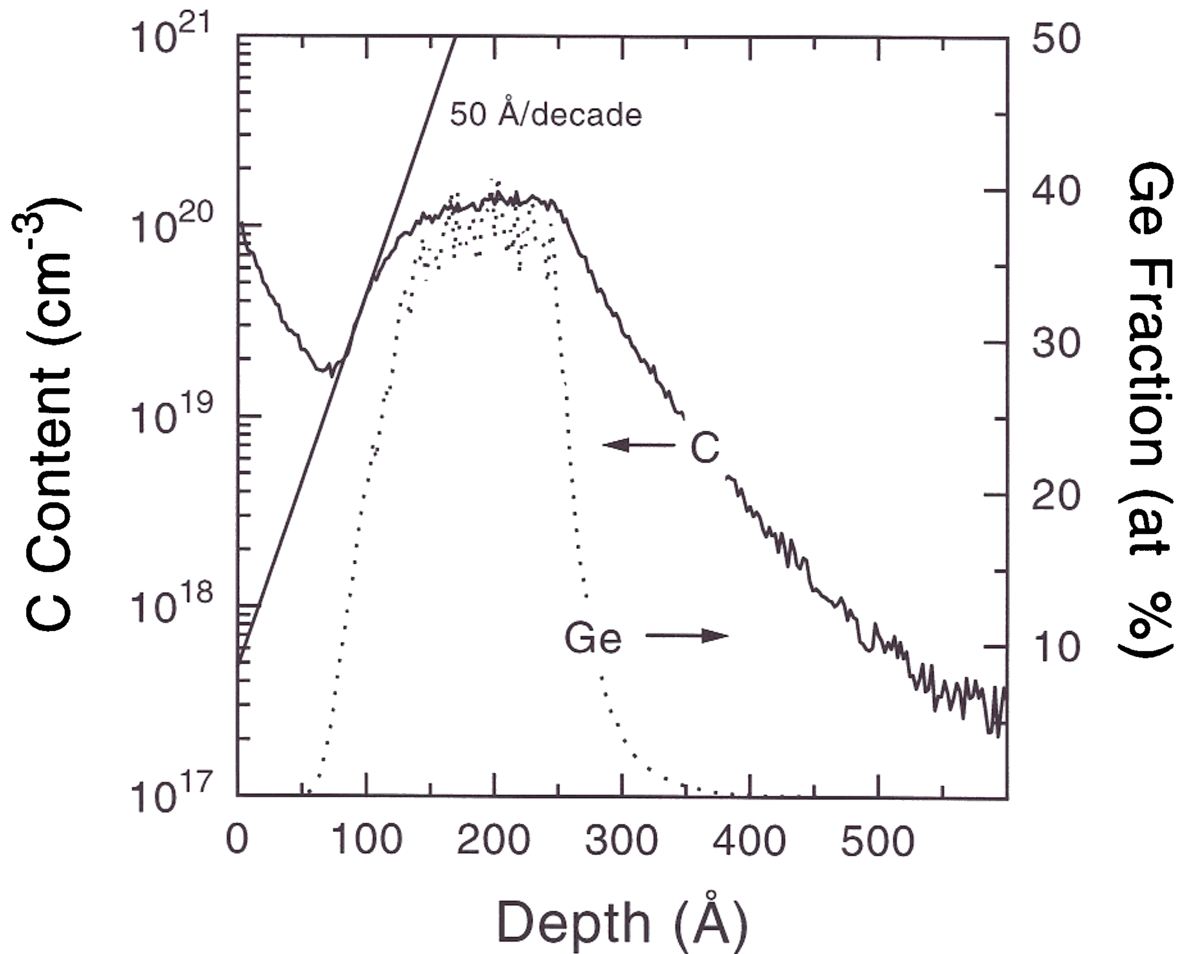

Figure 5.4: SIMS depth profile of $Si_{1-x-y}Ge_xC_y$. The primary ion bombardment was with low-energy Cs. The C content did not agree with that measured by XRD. The top interfacial slopes were 10 and 50 Å/decade for Ge and C, respectively.

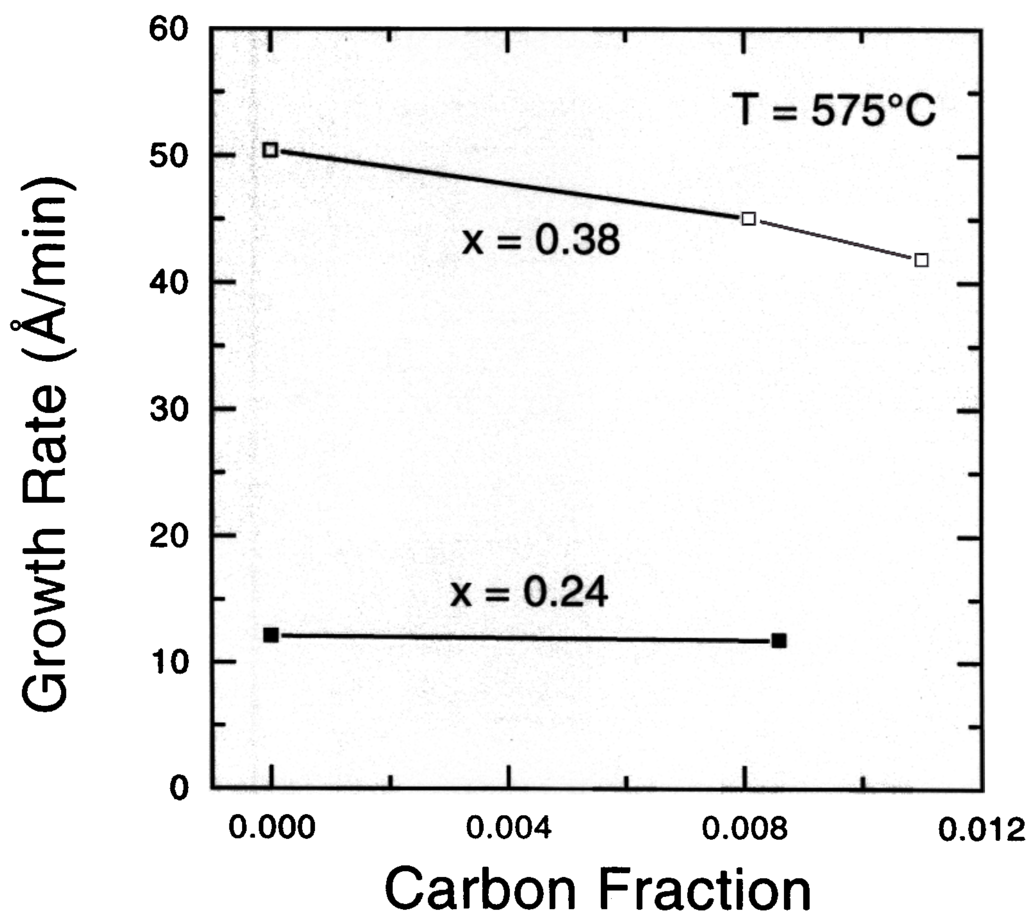

Figure 5.5: Growth rate as a function of C content for x=0.24 and 0.38. The film thicknesses were measured by the FWHM of the SIMS Ge profiles.

Chapter 6

Optical and Electrical Properties of $Si_{1-x-y}Ge_xC_y$

6.1 Photoluminescence Spectra

Photoluminescence (PL) was measured from two sets of samples with nominally undoped single, buried $Si_{1-x-y}Ge_xC_y$ quantum wells[73]. One set had $x = 0.24$ and a thickness $h = 120$ Å, the other $x = 0.38$ and $h =$ 160-190 Å. The maximum substitutional C concentration $[C_s]$, as measured by X-ray diffraction, was 1.1%. All samples were grown by RTCVD; the $Si_{1-x-y}Ge_xC_y$ layers were deposited at 575°C, and the ~100 Å Si caps were deposited at 675°C for 10 minutes. The samples received no thermal treatment after growth. The PL spectra were measured at 2, 25, and 77 K with a pump power density ~50 W/cm^2 from an argon ion laser. The luminescence was measured with a liquid nitrogen-cooled Ge diode using the standard lock-in technique. The spectra shown in Fig. 6.1 were measured by Yves Lacroix of Simon Fraser University and were normalized and corrected for the response of the experimental optical path.

These spectra are indeed $Si_{1-x}Ge_x$-like and exhibit no features other than the usual no-phonon (NP) and TO phonon replica peaks. There was a clear blueshift in these band-edge PL features as the C content was increased, indicating that adding C tends to increase the band gap of strained $Si_{1-x-y}Ge_xC_y$. As C was added the NP intensity increased relative to the TO intensity, suggesting enhanced alloy scattering

due to the C atoms in the lattice. The NP:TO peak intensity ratio for $x = 0.38$ and 25 K was fit by

$$\frac{I_{NP}}{I_{TO}} - 11 \cdot x(1-x) + 400 \cdot y(1 \quad y). \qquad (6.1)$$

This indicates that the alloy scattering matrix element of C atoms is more than an order of magnitude larger than that of Ge, which is not surprising in that the small C atoms cause a large local potential distortion compared to that of Ge. Also, note that the features in the 25 and 77 K spectra became narrower and weaker as C was added. This may have been due to reduced band filling caused by a lower carrier lifetime in the samples with C. For unknown reasons, the 2 K spectrum shown is broadened (FWHM=34 meV) compared to the control sample ($x = 0.24, y = 0$), which had a FWHM=12 meV at 2 K

The only previous report of band-edge photoluminescence in $Si_{1-x-y}Ge_xC_y$ by Boucaud *et al.*[80] showed some similarities to our results. In their measurements at 77 K on samples containing C, as in ours, high pump power density (~25 W/cm^2) was required to observe band-edge PL, and a superlinear pump power dependence was observed. At lower pump power density, their PL spectra were dominated by deep level luminescence of unknown origin about 250 meV below the $Si_{1-x-y}Ge_xC_y$ band gap. Also, they observed an additional luminescence band at high pump power when the band-edge PL was observed which was attributed to the D_3 dislocation line, casting doubt on the strain condition of their relatively thick films (800 Å).

6.2 Band Gap of $Si_{1-x-y}Ge_xC_y$

The band gaps of the $Si_{1-x-y}Ge_xC_y$ films were extracted from the PL spectra. The absolute band gap of the control sample with $x = 0.24$ and $y = 0$ was determined from its 2 K spectrum. The band gaps of the other samples were then determined by comparing the low-energy edge of their 77 K PL spectra to that of the control